Materials Today Bio 31 (2025) 101491

Contents lists available at ScienceDirect

Materials Today Bio

journal homepage: www.journals.elsevier.com/materials-today-bio

Deciphering cartilage neuro-immune interactions and innervation profile through 3D engineered osteoarthritic micropathophysiological system

Emine Kahraman [a,b,c], Daniela Vasconcelos [a,b], Beatriz Ribeiro [a,b], Ana Carolina Monteiro [a,b,d], Enzo Mastromatteo [e], Andrea Bortolin [a,b,c], Marina Couto [a,b,d], Laura Boschis [e], Meriem Lamghari [a,b], Estrela Neto [a,b,*]

[a] INEB – Instituto de Engenharia Biomédica, Universidade do Porto, Rua Alfredo Allen 208, 4200-135, Porto, Portugal
[b] i3S - Instituto de Investigação e Inovação em Saúde, Universidade do Porto, Rua Alfredo Allen 208, 4200-135, Porto, Portugal
[c] FEUP - Faculdade de Engenharia da Universidade do Porto, Rua Dr. Roberto Frias, s/n, 4200-465, Porto, Portugal
[d] ICBAS, Instituto de Ciências Biomédicas Abel Salazar da Universidade do Porto, Rua Jorge de Viterbo Ferreira 228, 4050-313, Porto, Portugal
[e] Trustech Innovation Technology, Via Baraggino, 76, 10034, Chivasso, Torino, Italy

ARTICLE INFO

Keywords:
Engineered cartilage
Osteoarthritis
Sensory innervation
Inflammation
Organ-on-chip

ABSTRACT

Osteoarthritis (OA) is an inflammatory musculoskeletal disorder that results in cartilage breakdown and alterations in the surrounding tissue microenvironment. Imbalances caused by inflammation and catabolic processes potentiate pathological nerves and blood vessels outgrowth toward damaged areas leading to pain in the patients. Yet, the precise mechanisms leading the nerve sprouting into the aneural cartilaginous tissue remain elusive. In this work, we aim to recapitulate *in vitro* the hallmarks of OA pathophysiology, including the sensory innervation profile, and provide a sensitive and reliable analytical tool to monitor the *in vitro* disease progression at microscale. Leveraging the use of patient-derived cells and bioengineering cutting-edge technologies, we engineered cartilage-like microtissues composed of primary human chondrocytes encapsulated in gelatin methacrylate hydrogel. Engineered constructs patterned inside microfluidic devices show the expression of cartilage markers, namely collagen type II, aggrecan, SOX-9 and glycosaminoglycans. Upon pro-inflammatory triggering, using primary human pro-inflammatory macrophage secretome, hallmarks of OA are recapitulated namely catabolic processes of human chondrocytes and the sensory innervation profile, supported by gene expression and functional assays. To monitor the OA micropathological system, a highly sensitive technology - EliChip™ - is presented to quantitively assess the molecular signature of cytokines and growth factors (interleukin 6 and nerve growth factor) produced from a single microfluidic chip. Herein, we report a miniaturized pathophysiological model and analytical tool to foster the neuro-immune interactions playing a role in cartilage-related disorders.

1. Introduction

Osteoarthritis (OA) is one of the most frequent musculoskeletal diseases, affecting approximately 600 million people worldwide, equal to 7 % of the global population and is foreseen to affect 1 billion people by 2050 [1]. OA is a complex inflammatory whole-joint disease, intrinsically characterized by cartilage damage and abnormalities of surrounding tissues of articular cartilage, such as subchondral bone, periosteum and synovium due to inflammation [2]. As a result of extracellular matrix (ECM) degradation and vascular invasion [3], sensory nerve fibers present in subchondral bone can sprout into the articular cartilage in human tibiofemoral OA and in tibial osteophytes [4]. While the sensory innervation of articular cartilage is acknowledged as a potential source of pain in patients with OA, the mechanisms underlying the sensory nerves growth and sprouting are unclear. To answer those disease-related biological questions and propose novel targeted therapeutics, animal models have been established to mimic OA [5]. Invasive, genetically modified and naturally occurring models of OA were developed, still, they do not allow investigation of all OA hallmarks due to anatomical and biological differences when compared to human pathology [5]. Therefore, to address these challenges, more robust *in vitro* models are under development to clarify the intricate mechanisms

* Corresponding author. i3S - Instituto de Investigação e Inovação em Saúde, Universidade do Porto, Rua Alfredo Allen 208, 4200-135, Porto, Portugal.
E-mail address: estrela.neto@i3s.up.pt (E. Neto).

https://doi.org/10.1016/j.mtbio.2025.101491
Received 23 April 2024; Received in revised form 15 November 2024; Accepted 12 January 2025
Available online 13 January 2025

underlying OA pathophysiology and, ultimately, to provide sustainable, long-term joint repair solutions for patients.

In this regard, organ-on-chip (OoC) platforms have been used to study different tissues/organs to recapitulate *in vivo* environment. This is followed by the development of multi-OoC models used to investigate the crosstalk between different tissues/organs through compartmentalization features where multiple cells can be cultured in single platform [6]. OoC platforms offer the possibility of using low amount of sample, cells, culture medium in a highly controllable microenvironment to create physiologically/pathologically reliable 3D microenvironments [7,8]. Up to this date, different joint tissue models have been reported using OoC technologies, namely synovium-on-chip, menisci-on-chip, OA-on-chip or combining more than one of those systems in one platform [9–18]. OA-on-chip was modeled through mechanical loading and/or biochemical stimuli on chondrocytes to mimic biomechanical environment of OA [12]. Although the relevance of the peripheral nervous system is acknowledged on OA progression [19], these models are lacking the importance of neuronal players, which are crucial to reveal the mechanism behind the neuroimmune profile and the OA-associated pain [20,21].

Along with miniaturized systems, analytical techniques must be adapted to sample size. Monitoring the information about the microenvironment and cellular behaviors from a single microfluidic device is still an enduring challenge in the field [22]. These limitations have led to a growing interest on biosensor integration into OoC and development of lab-on-a-chip (LoC) systems that can serve as sensitive and accurate read out of these *in vitro* systems [23,24]. This promising synergistic strategy offers higher sensitivity at low concentration of biological molecules, such as proteins and cytokines, that play a critical role on addressing the significant molecular players and mechanisms behind the pathophysiological conditions [25,26]. Up to this date, several groups have already established sensor-integrated OoC models for heart-on-chip devices to obtain contractile stress readouts [27] or muscle-on-chip to monitor IL-6 and tumor necrosis factor (TNF)-α (TNF-α) produced by murine skeletal myoblasts [28]. Similar approach can be applied also into joint-on-chip models to measure proinflammatory cytokines and other proteins from OA samples that can shed light on OA pathology. Despite all progresses achieved on OoC and biosensor technologies in recent years, there is still room for development of more practical platforms to assist cellular microenvironment monitoring and discovery of new targetable disease-specific biomarkers [25].

Herein, we aimed to develop an OA-like *in vitro* model to recapitulate the 3D architecture of native cartilage and address the innervation profile of cartilage under inflammatory conditions. We developed a 3D healthy cartilage construct encapsulating primary human chondrocytes in gelatin methacrylate (GelMA) hydrogel inside the microfluidic device and characterized the constructs' viability, morphology, phenotype, expression of ECM proteins and glycosaminoglycans (GAGs) content. To create the OA-like model, the healthy construct was exposed to proinflammatory macrophages' secretome. Afterwards, we showed that the OA-like model microenvironment promotes innervation through paracrine-secreted factors but not by direct coculture settings, supported by the balance between chemoattractant and chemorepellent axonal guidance cues expressed by the chondrocytes. To perform a quantitative and accurate analysis of the factors released to the OA-like model microenvironment, we developed a miniaturized LoC system, called EliChip™. EliChip™ is a microfluidic-based platform to provide miniaturized enzyme-linked immunosorbent assay (ELISA) that allowed the analysis of proinflammatory cytokines and growth factors from a single OoC. The combination of this technology with the OA-like model can open new opportunities for modelling *in vitro* cartilage-related disorders, boosting the development of more effective treatments and therapies. Our innovative approach has the potential to push forward the field of musculoskeletal research, ultimately leading to improved patient care and enhanced quality of life for those suffering from joint associated diseases.

2. Results and discussion

2.1. Mechanical characterization and biocompatibility of GelMA hydrogel

Different research groups have attempted to use wide range of hydrogel types to support chondrogenesis in 3D, namely: polyethylene glycol (PEG), collagen, fibrin, alginate, gelatin and their composites [29–34]. To date, GelMA has been widely used for cartilage tissue engineering applications owing to its easily adjustable rheological properties and being photocrosslinkable that allows to create 3D *in vitro* tissue models [34–39]. In this work, GelMA was used to support the patterning, 3D structures, and phenotype of cartilage-like engineered microtissues. To assess the best performing formulation, 5 % and 10 % (w/v) GelMA were tested regarding its mechanical properties and biocompatibility.

2.1.1. Porosity and swelling ratio of GelMA

To understand whether GelMA hydrogel would allow the diffusion of culture medium, that includes growth factors for chondrogenic differentiation, we analyzed the porosity and swelling ratio of 5 % and 10 % hydrogel concentration. The porosity and swelling ratio were calculated based on the solvent replacement method [40]. Our data showed that 5 % GelMA has higher porosity than 10 % GelMA at all time points (day 7, 14, 21 and 28) with significant differences at day 7 and day 14 (Fig. 1A). The results showed to be in accordance to Miri et al. reporting that 5 % GelMA has larger pore size when compared to 10 and 15 % GelMA hydrogels [41]. The higher crosslink density creates smaller but more complex meshes resulting lower porosity [42]. A similar trend was also observed in the swelling ratio assay. The swelling ratio of the 5 % GelMA was also significantly higher at day 7 and day 14 in comparison with the 10 % GelMA, with a similar trend on days 21 and 28 with no significant differences (Fig. 1B). These data demonstrated that increasing the concentration of polymer content results in the water absorption decrease due to lesser voids within the hydrogel structure.

2.1.2. Rheological properties of GelMA

The structural network of the hydrogels affects mechanical properties [43]. To evaluate the mechanical properties of the hydrogel, compression test was conducted using stress and relaxation mode. From the results of strain-stress curve, it was observed that the fracture stress of 5 % GelMA reached 60 Pa at 20 % strain where the linearity was observed, while 10 % GelMA reached 160 Pa at 20 % strain (Fig. 1C). This is due to higher crosslinking of 10 % GelMA, creating a solid networking, and resulting in a more steady structure and diminishing the effects of fluid content within the hydrogel [44]. Accordingly, the Young's modulus of the 5 % GelMA hydrogel was approximately 3 Pa whereas the Young's modulus of 10 % GelMA was 8 Pa (Fig. 1D). As it was previously described, higher Young's modulus is positively correlated with higher crosslinking density, level of polymerization and increased meshing structure [44]. Additionally, higher Young's modulus is a result of lower porosity with limited elastic buckling of the pore walls when the forces are applied to the GelMA hydrogel [45,46]. While divergent from the Young's modulus of native cartilage tissue (5.7–6.2 MPa), hydrogels with different stiffness (ranging from Pa to kPa) have demonstrated efficacy in supporting chondrogenic differentiation and facilitating the formation of new tissue [47–49]. GelMA has been widely used for cartilage tissue engineering applications owing to its easily adjustable rheological properties and photocrosslinkable features to create 3D *in vitro* tissue models [34–39] Taking all this into consideration, we move forward on chondrocyte and neuronal cell culture evaluation assessing cellular viability and morphology.

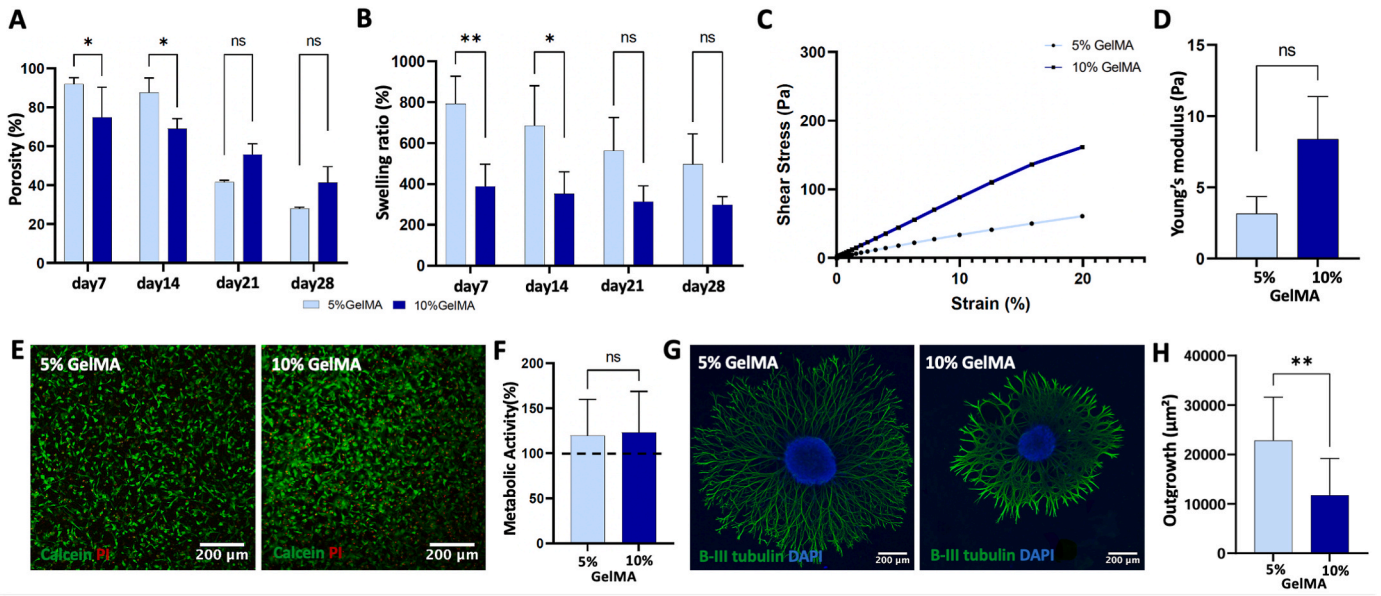

Fig. 1. *In vitro* mechanical characterization and biocompatibility of GelMA. **A.** Porosity measurements of 5 and 10 % GelMA hydrogels at day 7, 14, 21 and 28. **B.** Swelling ratio measurements of 5 and 10 % GelMA hydrogels at day 7, 14, 21 and 28. **C.** Compression test of 5 and 10 % GelMA showing their respective shear/stress curves. **D.** Young's modulus of 5 and 10 % GelMA calculated using their respective shear/stress curves. **E.** Cell viability of primary human chondrocytes encapsulated in 5 and 10 % GelMA and cultured for 7 days by live/dead staining (live cells: green; dead cells: red; scale bar = 200 µm). **F.** Metabolic activity of chondrocytes encapsulated in 5 and 10 % GelMA after 7 days of culture, evaluated through resazurin assay, relative to the 100 % control (3D chondrocyte pellet culture, dashed line). **G.** Representative images of axonal growth of DRG cultured on the 5 and 10 % GelMA for 5 days, n = 9 (beta-III tubulin: green; DAPI: blue; scale bar = 200 µm). **H.** Quantification of axonal growth area of DRG on the 5 and 10 % GelMA for 5 days. All comparisons were performed using Shapiro-Wilk test followed by Sidak's Multiple comparison test for A and B; Mann-Whitney test for D and H; unpaired parametric *t*-test for F. The statistical significance level was set to $p < 0.05$. For each assay n = 3, unless otherwise stated.

2.1.3. Biocompatibility of the GelMA

Prior to assemble the model comprising the cartilage and the nervous system, hydrogel biocompatibility was evaluated for both cell types, chondrocytes and sensory neurons. This was achieved through the assessment of chondrocytes viability, metabolic activity and morphology, as well as by quantifying the axonal growth of sensory neurons. Previous studies showed that cell viability might depend on the photoinitiator type, UV wavelength and intensity, independently from GelMA concentration [50,51], while photoinitiatior concentration (up to 0.5 % w/v) in 3D cultures does not cause significant loss of cell viability [52]. In line with those observations, we selected 0.2 % LAP to crosslink GelMA and a low intensity (10 mW/cm^2 at 365 nm) light source was chosen for the LAP mediated photocrosslinking to obtain high cell viability, in accordance to Fairbanks et al. [53].

The viability of human chondrocytes, after encapsulation in 5 and 10 % GelMA, was firstly investigated outside of the microfluidic device, using ibidi µ-Slide. After 7 days of culture the viability was assessed through Calcein-AM and propidium iodide (PI) staining. Qualitative assessment showed that cell viability on both concentrations of GelMA was maintained, with no differences among both groups throughout the culture time (Fig. 1E). We further checked the metabolic activity of the human chondrocytes encapsulated in 5 and 10 % GelMA hydrogels through resazurin assay at the same time point. The metabolic activity of human chondrocytes encapsulated in 5 and 10 % GelMA was calculated through resazurin assay, measuring the absorbance of resorufin, normalized to the cell number. We observed that both 5 and 10 % GelMA hydrogels did not impair the metabolic activity and no difference observed relative to the 100 % control (3D chondrocyte pellet culture, dashed line) (Fig. 1F). Regarding the impact on neuronal cultures, it is reported that GelMA hydrogels support simultaneous neuronal attachment and axonal growth of dorsal root ganglia (DRG) cells and Schwan cells [54]. To evaluate the impact of GelMA on mouse sensory neurons cultures, DRG were seeded on top of 5 and 10 % GelMA using ibidi µ-Slide, and axonal growth was afterwards assessed through immunostaining of beta-III tubulin (neuronal marker). The quantification of the total area occupied by neurites was performed as previously described [55]. We observed that the DRG cultured on 5 % GelMA had denser sprouting compared to 10 % GelMA (Fig. 1G). It is reported that hydrogel microarchitecture, namely porosity, can affect neuronal growth, differentiation, extension and branching [56], as cellular interconnectivity, nutrient and oxygen exchange are promoted [57]. In agreement with these reports, we observed an axonal outgrowth significantly higher for DRG cultured on 5 % GelMA when compared to 10 % GelMA (Fig. 1H).

After assessing the biocompatibility of the hydrogel for chondrocyte and DRG sensory neuronal cells, we selected 5 % GelMA as the most suitable hydrogel to provide the necessary microenvironment for both cell types. Therefore, we performed all the experiments within the microfluidic devices using 5 % GelMA hydrogel.

2.2. Microfluidic device characterization and patterning of chondrocytes in the device

2.2.1. Microfluidic design

In our group, models were developed to study peripheral bone innervation, coculturing sensory neurons and osteoblasts or osteoclasts [55,58–60]. Herein we used a microfluidic device to engineer cartilage microtissues and evaluate the impact of its secretome on sensory innervation profile. The device includes two compartments to replicate the *in vivo* architecture where the nerve terminals reach the peripheral tissues while the cell body is confined to the DRG near the spinal cord, allowing to model the *in vivo* physical barriers *in vitro*. Two distinct units are present: the nerve unit (somal side) and chondrocyte unit (axonal side) which are connected through microgrooves (450 µm length) that enable neurite growth (Fig. 2A). This device allows i. to culture sensory neurons derived from mouse DRG in the dedicated space on the somal side (3 mm punch) that facilitates the neuronal cells seeding, adhesion and decrease the shear stress during medium exchange; ii. to perform 3D

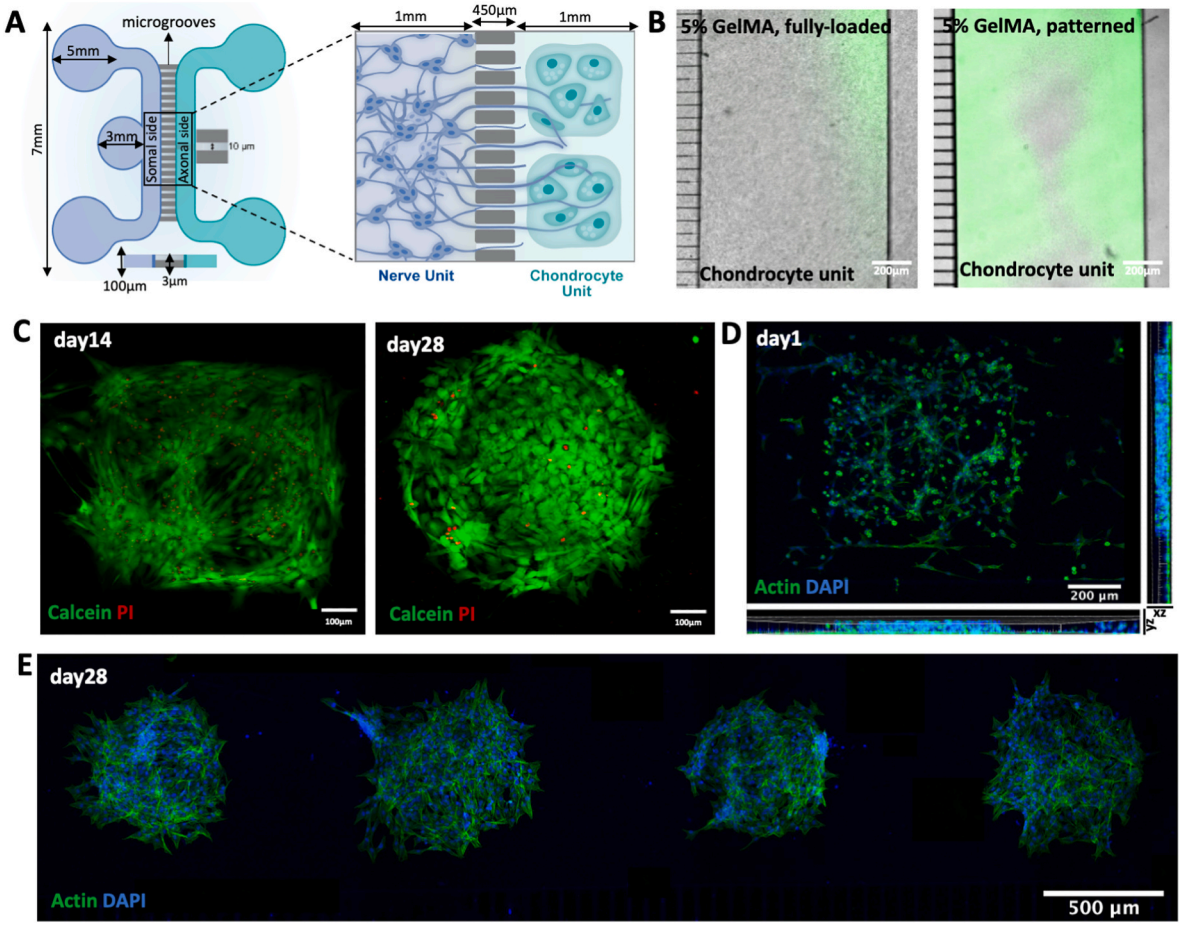

Fig. 2. Human articular chondrocytes micropatterning. **A.** Schematic representation of the microfluidic device comprising two compartments. On the left side, the nerve unit (blue) includes dissociated embryonic DRG neurons; on the right side, the chondrocyte unit (green) includes primary human chondrocytes encapsulated in 5 % GelMA. The two compartments are separated by microgrooves that allow the crossing of axons from nerve towards chondrocyte unit. **B.** Diffusion assay of FITC-Dextran through 5 % GelMA when fully loaded in the channel or patterned (scale bar = 200 µm). **C.** Cell viability of primary human chondrocytes encapsulated in 5 % GelMA and cultured inside the microfluidic device for 14 and 28 days (live cells: green; dead: red; scale bar = 100 µm). **D.** 3D pattern formation inside the microfluidic device showing morphology of the patterned chondrocytes (actin: green; nuclei: blue) and orthogonal projections (yz, xz) of the patterned chondrocytes using IMARIS software (scale bar = 200 µm; thickness of the pattern = 70 µm). **E.** Tilescan from 3D projection of the chondrocytes cultured for 28 days (actin: green, nuclei: blue; scale bar = 500 µm).

culture of primary human chondrocytes in chondrocyte unit (1 mm in width and 100 µm in height). The platform was assembled in a step-by-step manner, with each compartment being optimized prior to the complete model assembly.

2.2.2. *Evaluation of medium diffusion through microfluidic channels containing patterned vs fully loaded hydrogel*

To infer about the culture medium supply along the channel of the chondrocyte unit, diffusion of FITC-dextran (3–5 kDa) within the hydrogel was assessed. For this assay, two conditions were tested: i. the channel fully loaded with 5 % GelMA; ii. the channel including patterned hydrogel using the photomask (Fig. 2B). FITC-dextran solution (0.5 mg/ml in PBS) was added into the medium reservoirs, and the diffusion of the fluorescent dye was qualitatively evaluated by confocal microscopy based on the fluorescence intensity inside the compartment. It was observed that FITC-dextran diffuses immediately through patterns, whereas approximately 90 min were needed to diffuse through the fully loaded channel from beginning to the end of channel. This result indicates that presence of patterns inside the chondrocyte unit accelerates movement of fluid, which will improve the culture medium diffusion and nutrients supply to the cells in 3D.

2.2.3. *Patterning of chondrocytes inside the microfluidic device*

Human chondrocytes isolated from patients were encapsulated in 5 % GelMA and loaded inside the chondrocyte unit of the microfluidic device. Taking advantage of photocrosslinkable properties of GelMA, round and square shaped 3D cellular patterns were imprinted in the microfluidic channel. The viability of chondrocytes cultured inside the microfluidic platform for 14 and 28 days was assessed through Calcein-AM and PI staining. The culture time was defined to achieve full maturation of chondrocytes *in vitro* [61]. The results showed that cell viability was maintained at both time points, throughout fully chondrocytes maturation, independently of the geometric shape of the patterns (Fig. 2C).

We further evaluated the chondrocytes morphology and micropattern stability inside the microfluidic device, throughout the culture time. Morphological analysis showed that patterned human chondrocytes had heterogenous morphology, showing both round and elongated morphology at day 1 (Fig. 2D). Herein, 5 % GelMA with lower stiffness was used to support the generation of 3D engineered human cartilage microtissues in the microfluidic device. Li et al. showed that soft hydrogels (3 kPa) promote intercellular connectivity of bovine chondrocytes with heterogenous morphology [50]. Additionally, the 3D shaped imprinted chondrocytes in the channel were shown to be stable throughout the maturation period until day 28 (Fig. 2E).

2.3. Development of patient-derived tissue engineered constructs: healthy and OA-like model

2.3.1. Establishment of healthy human cartilage construct

To develop healthy cartilage constructs inside the microfluidic device, patient-derived primary human chondrocytes were encapsulated in GelMA and patterned using the previously defined parameters. To achieve the cell density required, chondrocytes were expanded after isolation. The cell culture conditions, in the presence of transforming growth factor beta 1 (TGF-β1), basic fibroblast growth factor (bFGF), and multiple passaging induce a process called dedifferentiation [62–64].

Dedifferentiated chondrocytes suffer morphological and phenotypic changes, becoming fibroblast-like cells with loss of Collagen type II (Col-II) and Aggrecan (ACAN) [64–67]. At 48h post-patterning no ACAN and Col-II were observed to be expressed by the 3D engineered constructs (Figure SI1). To secure the redifferentiation and chondrocytes maturation, patient-derived chondrocyte culture was maintained in chondrogenic medium, supplemented with TGF-β3. Chondrogenic and ECM-associated markers were analyzed at days 14 and 28 as indicators of early (SRY-Box Transcription Factor 9 (SOX-9)) and matured (ACAN, Col-II) stage of chondrogenic redifferentiation (Fig. 3A).

The expression of the ECM proteins namely ACAN (Fig. 3B), Col-II (Fig. 3D), and the transcription factor SOX-9 (Fig. 3F) was detected throughout the redifferentiation process (day 14); as well as throughout the maturation period (day 28) (Fig. 3C: ACAN; Fig. 3E: Col-II; Fig. 3G:

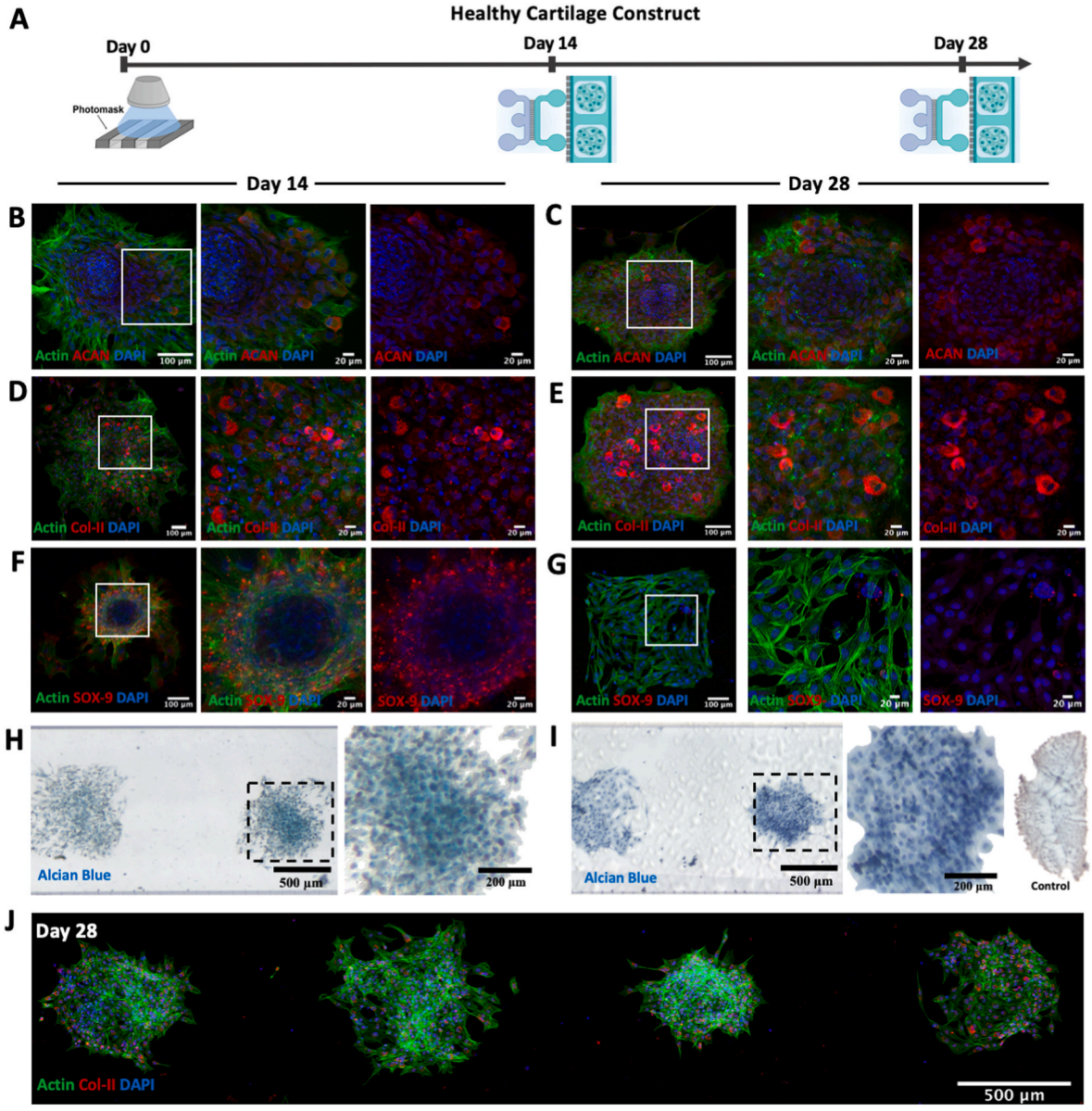

Fig. 3. Establishment of healthy 3D cartilage constructs in microfluidic devices. **A.** Schematic timeline of development of the healthy cartilage construct. Healthy construct is formed encapsulating chondrocytes in GelMA and crosslinked using a photomask. The healthy construct culture was maintained for 28 days, with an intermediate check point at day 14. **B-G.** Immunofluorescence analysis of chondrocytes encapsulated in 5 % GelMA for 14 days and 28 days, with their respective zoom-in images, showing ACAN, Col-II and SOX-9 (red), actin (green), nuclei (blue). **B.** Aggrecan (ACAN) at day 14, **C.** ACAN at day 28 **D.** Collagen-II (Col-II) at day 14, **E.** Col-II at day 28 **F.** SOX-9 at day 14 **G.** SOX-9 at day 28 (scale bar = 100 μm; 20 μm for each zoom-in images). **H.** Alcian Blue staining for GAGs (blue) produced by chondrocytes encapsulated in 5 % GelMA for 14 days and zoom-in image to a better visualization of the Alcian blue intensity (scale bar = 500 μm; 200 μm). **I.** Alcian Blue staining for GAGs (blue) produced by chondrocytes encapsulated in 5 % GelMA after 28 days and zoom-in image to a better visualization of the Alcian blue intensity (scale bar = 500μm; 200 μm). Control staining of GelMA without cells. **J.** Tilescan from 3D projection of the chondrocyte unit with Coll-II expression by patterned chondrocytes cultured for 28 days (scale bar = 500 μm); showing Col-II (red), actin (green), nuclei (blue).

SOX-9), respectively. The deposition of these cartilage specific ECM proteins can be seen with higher magnification of the specified areas. Lam et al. previously reported that chondrocytes encapsulated in GelMA initiated expression of ACAN and Col-II after 14 days of culture, indicating the initial cartilaginous matrices production [68]. Secretion of those proteins in cartilage ECM is important due to their role on regulation of cartilage regeneration [50]. While the expression of Col-II and ACAN at day 14 was kept towards day 28, we observed less SOX-9 expression at day 28 comparing to day 14. SOX-9 is reported as the first essential transcription factor that binds to specific sequences in COL2A1 gene to regulate chondrogenesis and production of ECM proteins [69]. SOX-9 expression levels are expected to stabilize during the chondrogenesis [70,71]. We further assessed the accumulation of GAGs, one of the main biomolecules synthesized by chondrocytes, through Alcian Blue staining at day 14 and 28. We observed an increase in the intensity of Alcian blue staining from day 14 (Fig. 3H) towards day 28 time point (Fig. 3I), an indicative of enhanced chondrogenesis. Additionally, Alcian blue staining of the empty hydrogel without cells showed that the hydrogel does not interfere with the staining (Fig. 3I). Occhetta et al. also reported an upward trend of GAGs expression relative to longer culture time (up to 14 days) of chondrocytes in microfluidic [12]. Although there are established cartilage microtissue models in microfluidic devices, maintaining the culture for the long term (28 days for full maturation of chondrocytes) remains challenging [12,14]. In this work, given the improved medium diffusion, high cellular viability, secretion of ECM structural proteins, we successfully develop a healthy cartilage microtissue model inside the microfluidic device stable for 28 days (Fig. 3J).

2.3.2. Macrophage secretome to induce cartilage proinflammatory conditions

There are several strategies to create proinflammatory environment on tissue engineered constructs *in vitro,* the most common being to expose the cells to proinflammatory cytokines. More specifically, it is highly common and well-documented the exposure of chondrocytes to TNF-α, interleukin (IL)-1β (IL-1β), and IL-6 to recapitulate the pathophysiological OA microenvironment [12,20,72]. With this approach, even though expression of the catabolic enzyme matrix metalloproteinases (MMP) 13 is increased, the use of proinflammatory cytokines alone (TNF-α, IL-1β, and IL-6) does not promote hypertrophy in human chondrocytes *in vitro,* as reported by Ferrao Blanco et al. [73]. To induce hypertrophy of human chondrocytes, they exposed chondrocytes to macrophages secretome taking advantage of factors secreted by macrophages [73]. In accordance, we decided to expose chondrocytes to proinflammatory macrophage secretome which provides a richer inflammatory environment to better mimic OA conditions. To do that, secretome was collected from human monocytes isolated from peripheral blood mononuclear cells (PBMCs), polarized into proinflammatory M1 macrophages under lipopolysaccharide (LPS) and gamma interferon (IFN-γ) stimuli. The M1 macrophage secretome was collected after 3 days of polarization as represented in Fig. 4A. Morphological evaluation of M0 macrophages proves that the cells remain round before the polarization (Fig. 4B), whereas heterogenous morphology was observed after the polarization (Fig. 4C), as defined in the literature [74]. Characterization and assortment of these heterogenous macrophage lineages was assessed through cell-surface markers and production of inflammatory mediators. The flow cytometry gating strategy was defined by selecting the $CD14^+$ cell population, as a general macrophage marker to define the cell of interest, followed by selecting M1 proinflammatory macrophage population through the expression of $CD86^+$ and HLA-DR+ (Fig. 4D). The flow cytometry results proved that polarization of monocytes into proinflammatory macrophages was successfully performed (Fig. 4D). The number of $CD86^+$ cells have coherently increased for each sample. Likewise, HLA-DR + cell population was significantly higher after the polarization in comparison to the cell population before stimulus. We further quantified the production of inflammatory mediators by ELISA before and after polarization and we observed higher expression of IL-6, TNF-α and higher IL-1β cytokines after polarization (Fig. 4E). As such, monocytes were successfully polarized into proinflammatory M1 macrophages and the macrophage secretome was characterized for further use in OA-like model.

2.3.3. Establishment of patient-derived OA-like model

The OA-like model was created by exposing the healthy 3D engineered cartilage construct to macrophage proinflammatory secretome mixed with chondrogenic medium (1:1). Chondrocytes were encapsulated and chondrogenic maturation was conducted towards day 28. When i. the healthy model reached day 12 or ii. the healthy model reached day 26, chondrocytes were exposed to proinflammatory environment and maintained under inflammation for 48 h (Fig. 5A). We first assessed the viability of chondrocytes through Calcein-AM and PI staining at day 14 and day 28. The results revealed that 48h exposure to proinflammatory M1 macrophage secretome did not impair cell viability at day 28 (Fig. 5B). In response to proinflammatory cytokines such as TNF-α and IL-1β, chondrocytes produce MMP13, a crucial enzyme involved in degradation of cartilage ECM components and GAGs, regulated by several signaling pathways, namely nuclear factor kappa-light-chain-enhancer of activated B cells (NF-κB) and mitogen-activated protein kinase (MAPK) [70,75,76]. Accordingly, we checked the breakdown/presence of GAGs in OA-like model and we observed that alcian blue staining was still present in the inflamed construct at day day28 (Fig. 5C), suggests that longer inflammatory stimulation might be required for GAG breakdown.

A panel of chondrogenic and inflammatory markers was evaluated to characterize key gene expression and phenotype changes between healthy 3D-engineered constructs and an OA-like model. Exposure of 3D-engineered chondrocytes to the M1 macrophage secretome resulted in a marked upregulation of inflammatory markers, including hypoxia-inducible factor 1-alpha (HIF-1α), C-C motif chemokine ligand 2 (CCL2), superoxide dismutase 2 (SOD2), IL-1β, and nitric oxide synthase 2 (NOS2), all of which are associated with the inflammatory state of chondrocytes (Fig. 5E).

Upregulation of NOS2 was shown to be a driver of OA-related chondrocyte dysfunction [77]. HIF-1α is recognized for its dual role in OA. While HIF-1α upregulates the pro-inflammatory cytokine IL-1β in osteoarthritic tissue, it might also support cartilage homeostasis in healthy conditions by maintaining chondrocyte function in hypoxic environments and increasing SOX9 expression [78,79]. In our study, the OA-like model demonstrated decreased SOX9 expression alongside elevated IL1β, suggesting that HIF-1α may be driving an inflammatory response in this context, thereby contributing to an OA-like phenotype.

C-C motif chemokine ligand 2 (CCL2), also known as monocyte chemoattractant protein-1 (MCP-1), is a chemokine crucial for recruiting monocytes and other immune cells to inflamed sites, thus amplifying the inflammatory response within joint tissues. Elevated levels of CCL2 have been identified in the synovial fluid of osteoarthritic knee joints, as well as following acute traumatic joint injuries. In animal models, CCL2 expression is induced in cartilage after surgical destabilization of the joint, and *in vitro* studies show it increases in response to mechanical injury of cartilage tissue. In addition to its role in immune cell recruitment, CCL2 directly affects pain pathways. It can directly excite nociceptive neurons, contributing to the pain associated with joint inflammation. Notably, transient upregulation of the CCL2/CCR2 axis in the dorsal root ganglia (and potentially within the joint itself) has been observed to precede the onset of pain, likely by increasing the sensitivity of joint tissues to mechanical stress [80,81]This suggests that CCL2 is an inflammatory marker and a mediator of nociception.

The expression of genes related to matrix degradation as a disintegrin and metalloproteinase with thrombospondin motifs 5 (ADAMTS5), and MMP1, MMP3, and MMP13 proteolytic enzymes showed to be increased from 3D engineered healthy constructs to the OA-like model (Fig. 5E). In line with our findings, others have reported that the production of MMP-

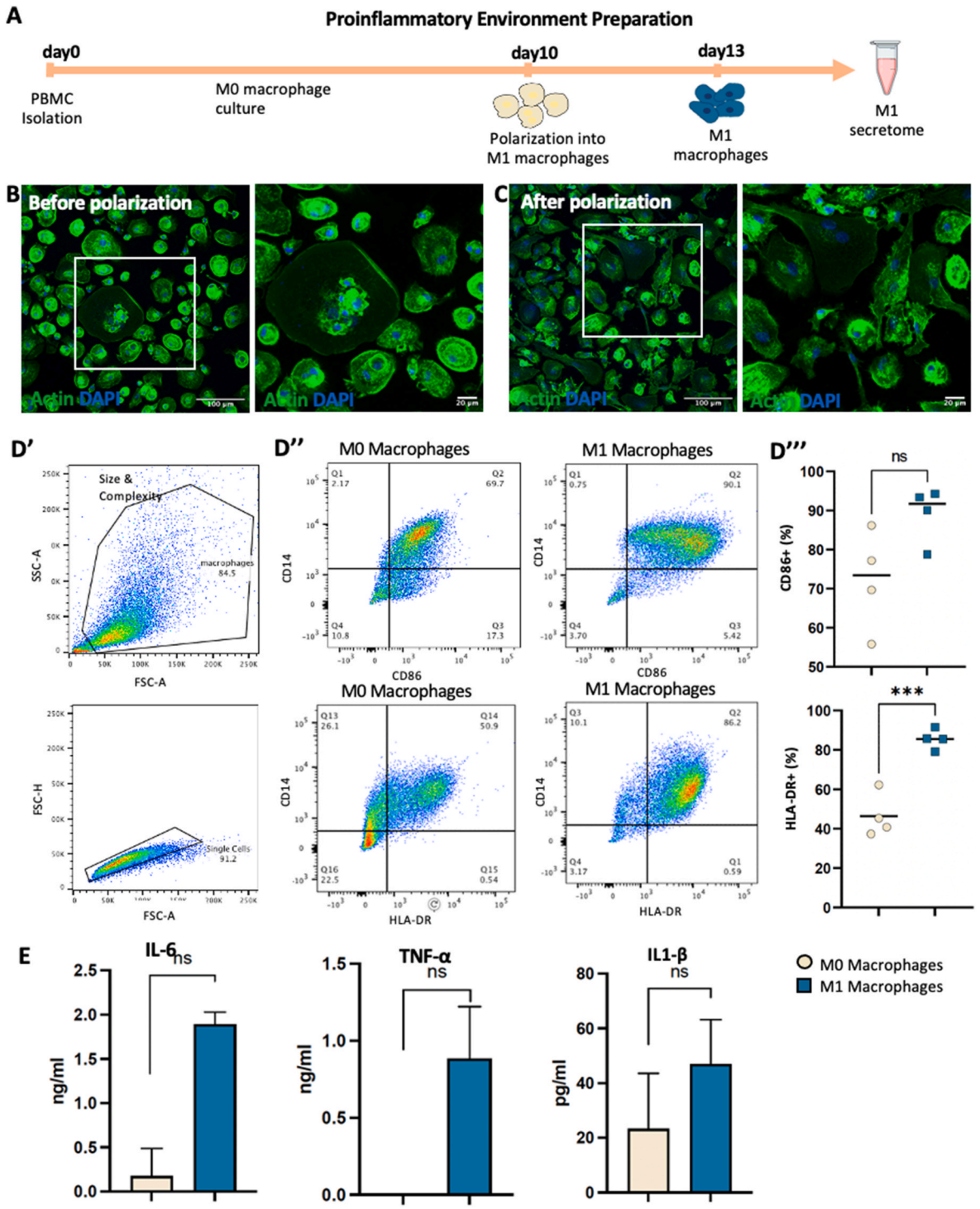

Fig. 4. Macrophage polarization towards M1 phenotype. **A.** Schematic timeline of proinflammatory secretome collection: monocyte isolation from peripheral blood mononuclear cells (PBMC) polarized into M1 proinflammatory phenotype through LPS and IFN-y treatment. **B.** Representative images of macrophages before polarization (M0 macrophages) and closer image with higher magnification **C.** Representative images of macrophages after polarization into M1 macrophages and closer image with higher magnification (actin: green; nuclei: blue; scale bar = 100 μm; 20 μm). **D.** Flow cytometry analysis of CD86 and HLA-DR positive M0 macrophages and M1 macrophages. D'. Cell gate defined with unstained samples, followed by single cell macrophage population ($CD14^{+}$) based on size and complexity. D''. M1 proinflammatory macrophage population through the expression of $CD86^{+}$ and HLA-DR+. D‴. Quantification of expressed CD86 and HLA-DR expressed by M0 macrophages and M1 macrophages (n = 4) (ns = non-significant, **p < 0,01). **E.** Quantification of proinflammatory cytokines (IL6, TNF-α, IL-1β) produced by M0 macrophages and M1 macrophages through ELISA. All the statistical analysis were performed using Shapiro-Wilk test followed by unpaired *t*-test for (IL6, TNF-α, CD86 and HLA-DR graphs; Mann-Whitney test for IL-1β graph. n = 4 for D‴. The statistical significance level was set to $p < 0.05$; ns = non-significant. n = 4 for D‴; n = 3 for E.

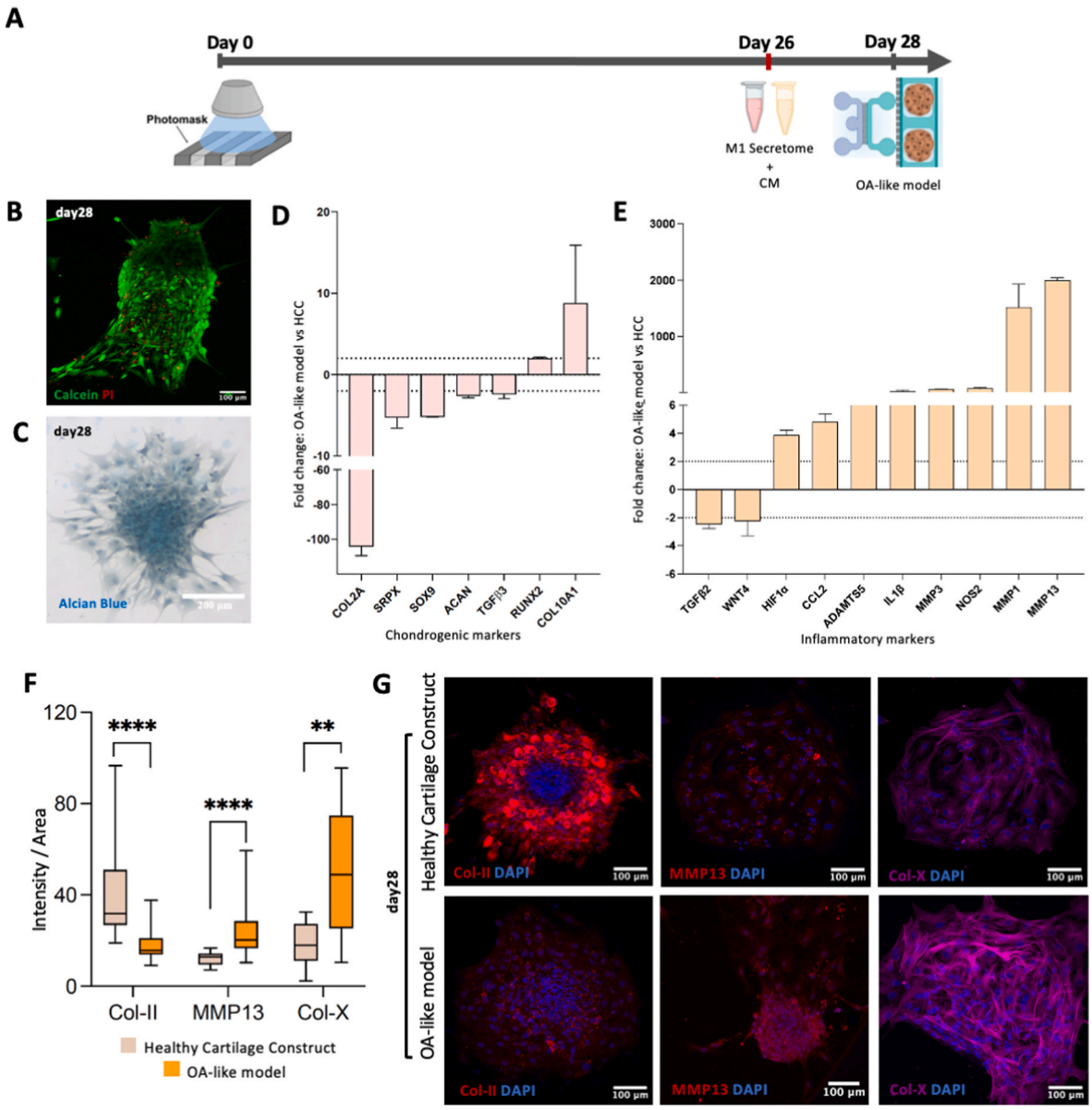

Fig. 5. Establishment of patient derived OA-like model **A.** Schematic timeline of development of the OA-like model. The cartilage construct was developed as healthy model and kept in culture until day 12 and day 26 in healthy state. Later, they were individually exposed to proinflammatory environment and maintained under inflammation for 48 h for further analysis. **B.** Calcein/PI staining of the chondrocytes after exposure of proinflammatory environment at day 28 (live cells: green, dead cells: red; scale bar = 100 μm); **C.** Alcian Blue staining for GAGs (blue) produced by chondrocytes following the proinflammatory treatment at day 28. **D.** Gene expression analysis of chondrogenic markers expressed by chondrocytes of the OA-like model and HCC. **D.** Gene expression analysis of catabolic reaction/inflammatory markers produced by chondrocytes of the OA-like model and HCC. **F.** Intensity/area quantification of expressed Col-II, MMP13 and Col-X proteins by HCC and OA-like model at day 28 (n = 5, 4 different donor) **G.** The representative immunofluorescence images of Col-II, MMP13; Col-X (red) and nucleus (blue). The statistical analysis was performed using Shapiro-Wilk test followed by Mann-Whitney test. The statistical significance level was set to $p < 0.05$.

1, −3, and −13 and aggrecanases ADAMTS−4 and −5 are stimulated by the combined expression of IL-1β and TNF-α [82]. Our data showed a loss of WNT4, which has been shown to induce spontaneous development of OA-like joint alterations in animal models [83] along with the decrease of TGF-β2 which also relates to a lower chondrogenic potential of cells.

Clear evidence on COL2A, sushi repeat containing protein X-linked (SRPX), SOX-9, ACAN and TGF-β3 reduction (≥2-fold decrease) was observed from healthy to inflammatory conditions with an increased expression of COL10A1 supporting the change towards a hypertrophic phenotype of OA-like 3D engineered constructs. In fact, these data were further supported by the quantitative analyses of the protein expression by immunohistochemistry. We assessed the expression of Col-II, MMP13, and Col-X proteins in both the healthy construct and OA-like model at day 28. Our findings showed that chondrocytes in the OA-like model consistently exhibited reduced Col-II production, along with increased MMP13 and Col-X protein expression, compared to chondrocytes in the healthy construct (Fig. 5F and G). These results indicate that our OA-like model successfully replicates a key hallmark of osteoarthritis, specifically the loss of ECM components like Col-II and increased MMP13 secretion [84,85]. Additionally, Col-X expression shows a shift toward a hypertrophic phenotype in the chondrocytes within the 3D-engineered OA model (Fig. 5F and G).

2.4. Impact of OA-model on sensory innervation profile

2.4.1. Paracrine signaling: 3D engineered OA-model secretome on sensory innervation profile

Unlike other musculoskeletal connective tissues, namely periosteum and synovium, cartilage lacks blood vessels and innervation supply. However, studies acknowledged that nerve fibers, branching from subchondral bone, reach cartilage tissue in OA settings [2], playing a major role in the inflammation and OA-associated pain [19]. Still, the mechanisms regulating the neuronal sprouting are unclear. Neuro-immune modulation is accepted as a crucial component for the OA mimicking platforms to study the interplay between the peripheral nervous system (PNS) and joint tissue [86]. Building on above mentioned cutting-edge technologies and knowledge, we integrated sensory neurons in the nerve unit of the microfluidic device and exposed the axonal terminals to the secretome of healthy and inflamed 3D engineered cartilage constructs. As such, we aimed to evaluate the axonal growth of DRG neurons in response to the developed model to functionally recapitulate aneural native cartilage tissue and the innervated OA-like microenvironment [86,87].

In this model, we cultured dissociated sensory neurons from DRG in the presence of the healthy and inflamed 3D engineered cartilage constructs secretome on the axonal side (chondrocyte unit) of the device (Table 1, Fig. 6A). The healthy and inflamed OA-like models were developed as previously defined and their secretome were collected at day 28. Then, dissociated sensory neurons terminals were exposed to healthy and inflamed construct secretome and their control groups; namely chondrogenic medium (CM) as a control to healthy construct secretome (HC-S), macrophage secretome mix (MS) (1:1, chondrogenic medium and M1 macrophage secretome) as a control to inflamed construct secretome (OA-S) (Fig. 6A). When sensory neurons were exposed to HC-S, we did not observe any axonal growth towards axonal side of the device (Fig. 6B). In contrast, when sensory neurons were cultured with OA-S, an increased axonal growth was observed towards the inflammatory microenvironment (Fig. 6C). The quantification of axonal growth was assessed using AxoFluidic, an algorithm previously developed by our group [88]. In the graph, λ value represent the length of the axons, while A value represent the number of axons that cross to axonal side of the device. The analysis shows that in presence of OA-S, there is a significant increase in the length of axons and in the number of axons that reaches the chondrocyte unit of the device in comparison with HC-S (Fig. 6D). In comparison to healthy model (HC-S), the inflammatory construct (OA-S) might secrete neuro attractant factors released by inflamed chondrocytes promoting innervation towards axonal side of the device, whereas healthy chondrocytes secrete nerve repellent factors.

When neurons were cultured with CM, without contact with chondrocytes, we observed that neurites were thoroughly able to cross microgrooves towards the axonal side of the device, proving that the medium alone does not impair axonal growth (Fig. 6E). We further quantified the axonal growth of sensory neurons and we demonstrated that there was a significant increase on the neurite sprouting, and the number of axons crossing, towards CM comparing to HC-S (Fig. 6F). Previous studies showed that sodium pyruvate and insulin, components of CM formulation, promote viability of neurons, neurite length and number of branching of cultured dissociated mice DRG neurons [89,90]. We confirmed that, by eliminating these factors from the CM, no growth was observed (data not shown). Comparing to CM experimental control, our data indicate that neurons exposed to HC-S are subjected to a neuronal repulsion, recapitulating the native cartilage tissue lacking innervation supply. The further comparison of the impact of OA-S and MS on sensory innervation shows significantly higher λ and A values when sensory neurons cultured with OA-S than the neurons cultured in the presence of MS (Fig. 6G and H). We successfully recapitulate the innervation profile of healthy and inflamed cartilage by assessing axonal outgrowth of sensory neurons. These data strengthen our hypothesis that the secretomes from HC-S and OA-S comprise different combinations of axonal guidance cues, e.g., semaphorins, which have a crucial role on specific axon guidance for sensory nerve fibers in joint [91,92]. Additionally, it has been described that catabolic pathways of chondrocytes induced by inflammatory environment can possibly guide innervation of substance P positive nerve fibers towards the inflamed cartilage [2]. This breakdown of cartilage homeostasis stimulate release of IL-1β and MMP13 in human articular chondrocytes and these accelerated catabolic processes promote ingrowth of nerve fibers into the articular cartilage [2,93].

2.4.2. Direct signaling: 3D engineered OA-model coculture with sensory neurons

To deepen our understanding of the crosstalk between 3D engineered cartilage and sensory neurons, we additionally evaluated the two-way, real-time and bidirectional interactions between sensory neurons and chondrocytes on a single platform, through coculture experiments (Fig. 7). Direct coculture experiments offer contact between the different cell types, enabling communication through the cells' surface receptors and gap junctions, while keeping the local communication through soluble factors released by the cells [94]. The 2-compartment microfluidic device guarantees the analyses of axonal responses of sensory neurons to different biochemical stimuli originating from healthy and inflamed 3D engineered cartilage constructs in real-time, similar to previously established compartmentalized microfluidic models for other tissue types, except cartilage [95].

The developed 3D engineered cartilage constructs, under both healthy and OA-like environments, were cocultured with dissociated sensory neurons derived from mice DRG, to evaluate how the constructs impact the sensory innervation profile. The 3D engineered constructs were allowed to reach full maturation until day 23 when they were exposed to M1 macrophage secretome (MS) for additional 48h. Dissociated sensory neurons were seeded in the nerve unit and the coculture proceeded for 5 days until day 28 of chondrocyte maturation (Fig. 7A). At day 28, upon the 5 days coculture, the 3D cartilage constructs were stable showing the expression of Col-II (Fig. 7E, healthy cartilage construct) and MMP-13 (Fig. 7E, OA-like model). Contrary to the data obtained for the paracrine effect mediated by the different secretomes, both coculture with 3D healthy cartilage construct and 3D engineered OA-like model did not increase the axonal growth of sensory neurons (Fig. 7B and C). In fact, for both conditions, images showed that sensory neurons do not project their axons toward the chondrogenic unit where the patterns were cultured. To discard the possible impact of GelMA hydrogel on the axonal growth, sensory neurons were cultured in the presence of empty hydrogel patterned in the chondrogenic unit. Great axonal growth was detected, showing the neurites surrounding the GelMA patterns, with no signs of axonal degradation (Fig. 7D).

To understand the molecular mechanisms underlying the repulsive axonal behavior mediated by 3D engineered constructs, we analyzed the

Table 1
Media composition description used to set the experimental conditions for paracrine effect studies of healthy and inflamed 3D engineered chondrocytes on sensory neurons.

CM	Chondrogenic medium
Complete media used to culture the 3D engineered chondrocytes. This media has not been in contact with cells.	
HC-S	Healthy construct-secretome
Secretome collected from 3D engineered chondrocytes upon culture with CM (standard culture conditions - healthy).	
MS	Macrophage secretome mix
Medium composed by M1 macrophage secretome + CM (1:1). This formulation is composed by a mixture of secretome collected from M1 macrophages and chondrogenic medium (CM).	
OA-S	OA construct-secretome
Secretome collected from the 3D engineered constructs after exposure to MS (inflammatory conditions triggered by the MS stimuli).	

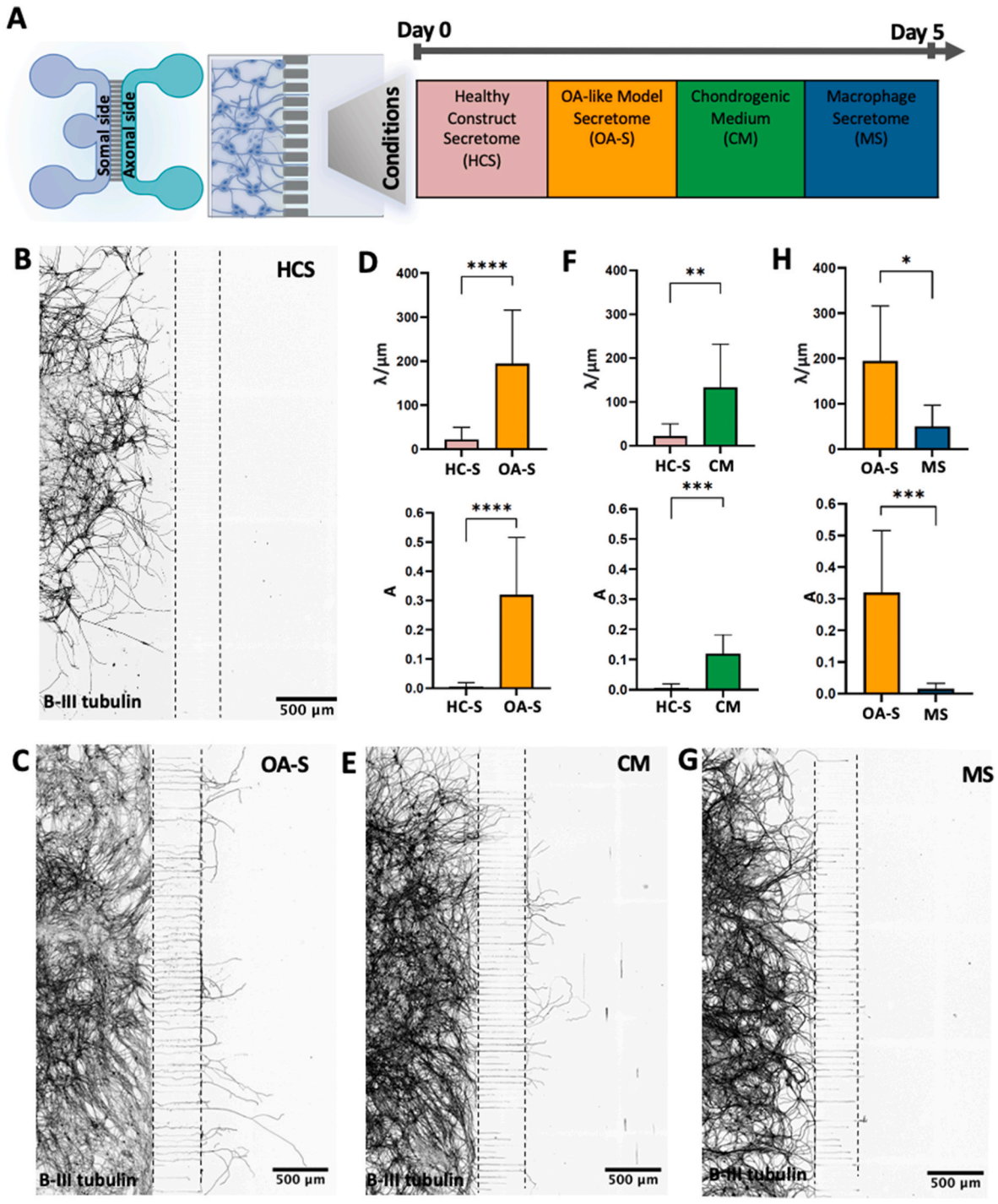

Fig. 6. Impact of healthy *vs.* inflamed cartilage construct secretome on axonal growth **A**. Schematic explanation of the experimental groups, where dissociated DRG were cultured in the microfluidic device and exposed to healthy construct secretome (HC-S): pink, OA-like model secretome (OA-S): orange, chondrogenic medium (CM): green, macrophage secretome (MS): dark blue, on the axonal side of the device. **B**. Beta-III tubulin staining of dissociated DRG neurons cultured with HC-S. **C.** Beta-III tubulin staining of DRG neurons in the presence of OA-S in axonal side of the device (scale bar = 500 µm). **D.** Quantification of axons showing sprouting of axons and number of axons that reaches the axonal of the device in presence of OA-S comparing to HC-S, n = 11 for HC-S; n = 11 for OA-S. **E.** Beta-III tubulin staining of DRG neurons in presence of CM **F.** Quantification of axonal growth in presence of HC-S comparing to CM, n = 6 for CM. **G.** Beta-III tubulin staining of neurons when they were cultured in the presence of MS **H.** Quantification of axonal growth in the presence of OA-S and MS, n = 4 for MS. Axonal growth of sensory neurons was quantified using AxoFluidic. λ value represents the extension of axons in the microfluidic device, while A value represents the axons that cross the microgrooves the chondrocyte unit of the microfluidic device. All the statistical analysis were performed using Shapiro-Wilk test followed by Mann-Whitney test. The statistical significance level was set to $p < 0.05$.

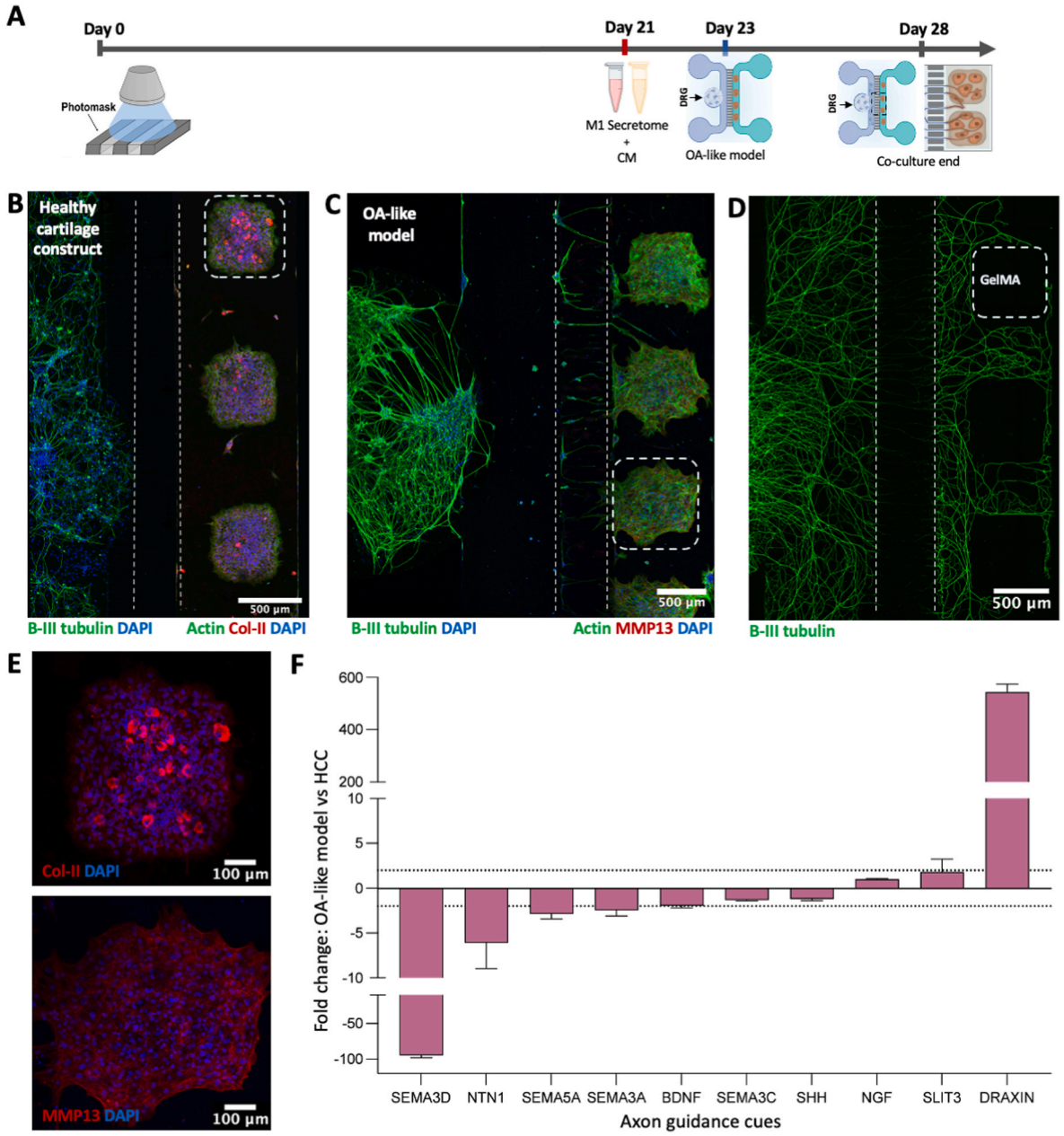

Fig. 7. Coculturing of sensory neurons and 3D engineered healthy cartilage construct (HCC) and OA-like model in two compartment microfluidic device. **A.** Experimental timeline of the coculture model. **B**. Immunofluorescence analysis of sensory neurons and chondrocytes, in presence of HCC on the chondrocyte unit of the device, showing B-III tubulin (green), nuclei (blue) for axons; Col-II in (red), actin (green), nuclei (blue) for chondrocytes. **C.** Immunofluorescence analysis of sensory neurons and chondrocytes, in presence of OA-like model on the chondrocyte unit of the device, showing B-III tubulin (green), nuclei (blue) for axons; MMP-13 (red), actin (green), nuclei (blue) for chondrocytes. **D.** B-III tubulin staining axons of dissociated DRG neurons when cultured with patterned 5 % GelMA, without chondrocytes (empty) **E**. Zoomed image of the marked patterns, showing Col-II expressing chondrocytes on HCC; MMP-13 expressing chondrocytes on OA-like model. **F.** Gene expression analysis of axon guidance cues expressed by chondrocytes of the HCC and OA-like model. (Scale bar = 500 µm; 100 µm).

expression levels of axon guidance cues with a consolidated capability in promoting axonal growth or repulsion. The gene expression analysis showed that semaphorins (Sema3A, 3C, 3D and 5A) were reduced from healthy to OA-like model (Fig. 7F). Semaphorins are secreted proteins known to function as chemorepulsive agents inhibiting axonal outgrowth [92,96]. The higher expression of these molecules by the healthy 3D engineered cartilage supports the data collected from both paracrine secretome assay and the coculture assay. Netrin-1 (NTN1) was also shown to be downregulated in the OA-like model. This protein can play a dual role in the axonal growth [97], however in the context of OA, it was shown to be expressed by the osteoclasts present in the joint tissue to promote axonal growth [98]. In this 3D engineered OA-like model the reduction of netrin-1 and brain-derived neurotrophic factor (BDNF), along with the increased expression of repulsive slit homolog 3 (SLIT3) and draxin molecules support the functional axonal growth data obtained from the direct coculture settings [99,100]. Previous studies already established the inhibitory effect of slits and draxin on axonal outgrowth both for central and peripheral nervous system, including sensory neurons [101–103]. Besides the impact on axonal guidance, slit3 has been linked to a regulatory role in endochondral ossification by β-catenin suppression in chondrocytes [104]. While no data has been published on the draxin expression by chondrocytes, the deleted in colon carcinoma (DCC) receptor that binds draxin and netrin-1 was shown to be specifically up-regulated in chondrocytes of OA patient samples

compared with healthy patients [105]. Besides the role of these axon guidance cues on neuronal regulation, their impact is also described on chondrocytes differentiation, migration and expression of catabolic markers [105].

In the direct coculture assays, it is essential to account for the dynamic nature of soluble factors, particularly those with shorter half-lives or that require elevated local concentrations to impact nearby cells effectively. Their influence might be significantly underrepresented in secretome assays, where samples are collected and analyzed at static time points. In a coculture environment, however, these factors are continuously secreted, facilitating a sustained and localized signaling effect. This continuous interaction allows for a different assessment of how these molecules influence cell behavior, as their transient presence can play critical roles in modulating responses such as axon guidance and inflammation. Thus, interpreting the functional assays from coculture setup alongside paracrine secretome testing can provide a fuller understanding of cell-cell interactions that are essential for modeling complex, multicellular environments like the joint.

2.5. Quantitative monitoring of engineered microtissue in the microfluidic platform

The quantitative analysis of the microfluidic platform stands as a hallmark in advancing the development of OoC systems, providing invaluable insights into the dynamic behaviors of the miniaturized pathophysiological models. However, it remains notably challenging achieving precise quantification in this cutting-edge field. One of the most commonly used technique for protein and cytokine detection is based on immunoassays, ELISA and antibody array assays [106,107], which generally are incompatible with miniaturized OoC systems given the low volume and concentrations of factors secreted within the microfluidic platforms. This challenge drives the rationale for the fabrication of a sensitive top-level LoC sensor to monitor the engineered microtissue system.

2.5.1. Principle and design of EliChip™ system

To overcome the need of pooling samples decreasing the data statistical power, we provide a highly sensitive technology relying on specific antibody-antigen interactions, with the use of 10 times less volume than the standard ELISA. EliChip™ is a portable and off-chip automated Lab-on-a chip (LoC) system, developed to provide miniaturized ELISA allowing the sample analysis from a single OoC for point of care enzyme immunoassays (patent no. WO2018015931). The system is based on a disposable microfluidic card and a reader for handling reagents and reading the results. It allows non-specialized personnel to perform quantitative low-cost analysis on single sample.

The EliChip™ LoC has 4 reaction lines made up of different reservoirs to store reagents, a reaction chamber, a detection chamber and a waste reservoir The reagent storage region comprises one or more reagent micro-reservoirs adapted to contain the reagents necessary for

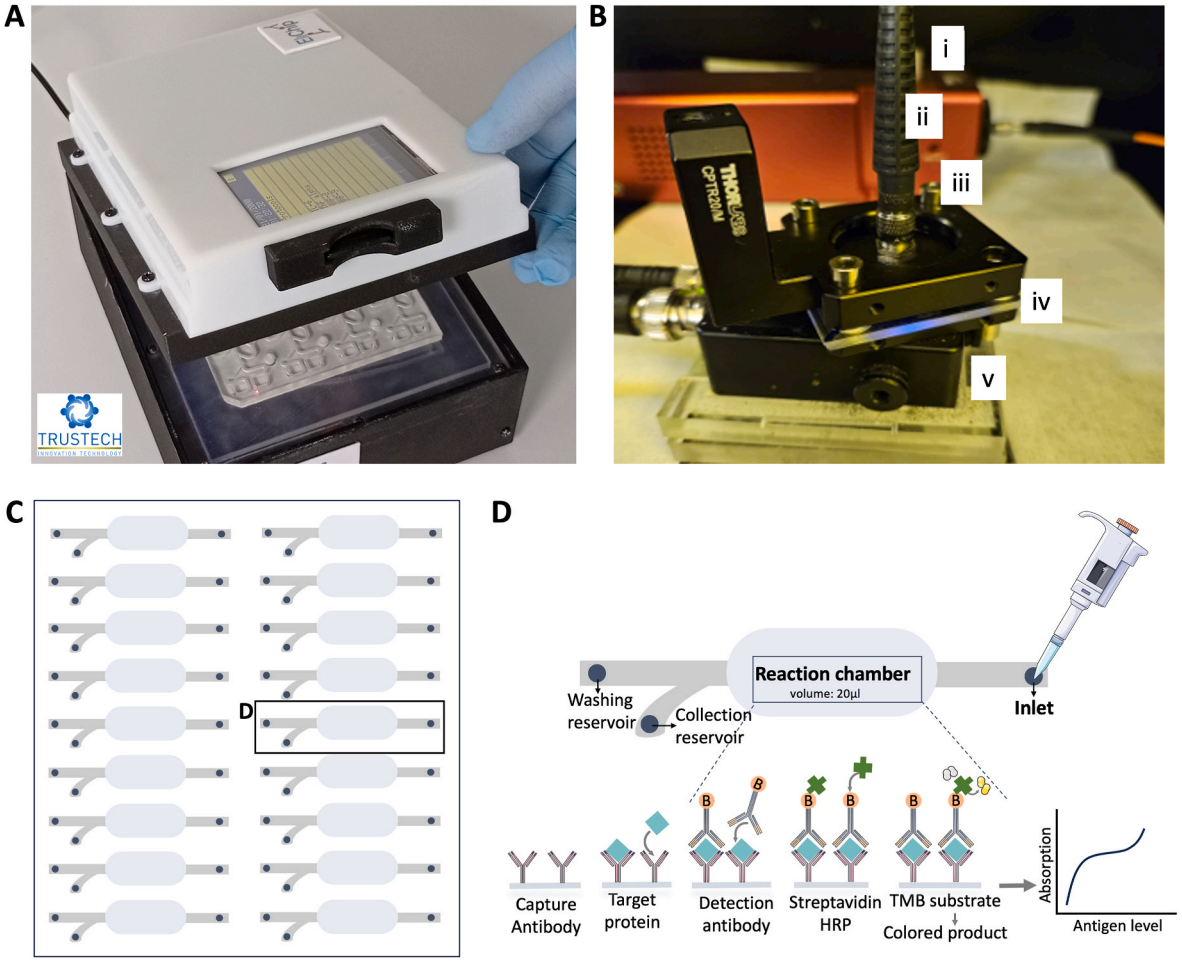

Fig. 8. Design of the lab on a chip (LoC) for protocol set up and working principle. **A.** EliChip™ reader with the LoC cartridge inside. **B.** Optic reading module: i) halogen lamp; ii) Optical fiber; iii) Interface between LoC and the module; iv) LoC; v) the photo diode. **C.** The disposable microfluidic card designed to include 18 parallel circuits. **D.** Schematic representation of the functional unit of each circuit in the card, composed of a washing and a collection reservoir, a reaction chamber and an inlet. Antibody-antigen conjugation occurs in the reaction chamber, following the working principle: the coating of the chamber with capture antibody is followed by target protein and detection antibody interaction and finally, HRP-TMB reaction gives the final-colored product to measure antigen level.

conducting the assay (e.g., conjugated antibodies, enzymes, chromogenic reagents, washing solutions, buffer solutions and acids) suitably preloaded and ready to use to avoid any possibility to contaminate the reader. All these areas are connected with a microfluidic circuit. Analytical protocols are completely managed by the automated portable instrument/reader (Fig. 8A).

To develop the protocols, a new LoC was designed with 18 simplified microfluidic circuits (Fig. 8C). With this alternative LoC design only part of the channels and the reaction chamber of EliChip™ disposable LoC were retained (Fig. 8D). In this case the loading of sample and reagents is manual, while the reading is carried out with the EliChip™ reader. This LoC is useful to optimize the analytical protocol of the target molecules with minimal reagent consumption. The region of insertion of the sample to be assayed (with a volume of 20 μl) receives the liquid sample containing the analytical of interest such as, for example, cytokines and growth factors present in cells secretome. The reaction region, containing immobilized probes where the immunoenzymatic reaction occurs, is pre-coated with the capture antibody, followed by i. binding target protein to the capture antibody and to the detection antibody; ii. HRP-TMB conjugation in the reaction region that will produce a final-colored product through oxidization of TMB (Fig. 7B). The final-color intensity is correlated with the antigen level in the sample. The chamber was conceived to prevent air bubbles forming and to provide reproducible results. The colored solution is placed in a reading chamber, specifically designed to interface the optical module. Interface region with the instrument is possible through connections that put the microfluidic circuit present the LoC in communication with the management and analysis instrument. A protective film for closing the inlets/outlets (when the LoC is not used), allow the preloaded LoC to be provided while preventing the evaporation of liquids or any contamination.

The hardware and software to control the fluidics, read the results and send the data, can be assessed independently locally and/or remotely. The reading, in the set-up phase can be carried out both through an external optic module and through EliChip™ reader. The optic module is composed of a halogen lamp as light source filtered at 450 nm and a photodetector (Fig. 8B). Instead, in EliChip™ reader, the optical module consists of 4 white LEDs interfaced with 4 CMOS mini-spectrometers with 11 reading lines. The great advantage of EliChip™ is that it can read multiple wavelengths and therefore allows the use of different tracers. The software interface allows quickly interchange between optimized protocols depending on the analyte under assessment.

2.5.2. *Off-chip automated LoC system for soluble factors*

EliChip™ LoC system technology was assessed by testing two different cytokines (IL-6 and TNF-α) and a growth factor (nerve growth factor, NGF). The quantification range and limit of detection (LoD) allowed to infer about the sensitivity of EliChip™. A maximum concentration of 500 pg/mL for IL-6 and NGF, and 2000 pg/mL for TNF-α, were validated within the linearity of the calibration curve regression. An LoD of 11.80 pg/ml, 30.03 pg/ml and 11.20 pg/ml was set for IL-6, TNF-α and NGF, respectively (Table 2). Commercially available standard ELISA assays have a maximum concentration in different ranges: for IL-6 and TNF-α: 500 pg/ml (ELISA MAX™ Deluxe Set Human TNF-α, cat no. 430204; ELISA MAX™ Deluxe Set Human IL-6, cat no. 430504, Biolegend); for NGF: 1750 pg/ml (ELISA® Human beta nerve growth factor, cat no. ab193760, ABCAM), whereas LoD are 7.8 pg/ml for IL-6 and TNF-α, and 27.3 pg/ml for NGF (Table 2). Considering such values, EliChip™ offers higher sensitivity for NGF detection when compared to commercial ELISA kits given that some of the samples contained NGF at a concentration of 13 pg/ml (lower than the LoD of the commercial ELISA kit) which precluded its detection from the chondrocyte secretome. Even though EliChip™ has higher LoD for IL-6 and TNF-α, the LoC technology offers the unvaluable possibility to obtain read out from a single OoC device, eliminating the need of high volumes for immunoassays.

Table 2
Optimized detection range of each molecule (IL-6, TNF-α and NGF) and respective limit of detection (LoD) for EliChip™ and standard ELISA.

Analyte	EliChip™		Standard ELISA	
	Range (pg/ml)	LoD (pg/ml)	Range (pg/ml)	LoD (pg/ml)
IL-6	0–500	11.80	0–500	7.8
TNF-α	0–2000	30.03	0–500	7.8
NGF	0–500	11.20	0–1750	27.3

Intra-assay coefficient of variation (intra-assay CV%) and inter-assay coefficient of variation (inter-assay CV%) relates to the precision and accuracy of the assay. The average intra-assay CV% (standard deviation/mean x 100) was calculated by confronting 2 triplicates for each concentration on the same card. The inter-assay CV% was calculated by confronting 10 analyses performed on 10 different cards. An average intra-assay CV% of 3.39 %, 9.94 % and 5.93 % was detected for IL-6, TNF-α and NGF, respectively (Table 3). The average inter-assay CV% for IL-6, TNF-α and NGF were 4.76 %, 3.51 % and 5.75 %, respectively (Table 3). Overall, the protocols optimized for EliChip™ show good sensitivity and reproducibility (Tables 2 and 3).

A side-by-side validation of the EliChip™ compared to standard ELISA was performed quantifying the secretion of IL-6 by M0 macrophages and M1 macrophages. Conventional ELISA with a range of detection between 7.8 and 500 pg/mL and a sensitivity of 4 pg/mL (ELISA MAX™ Deluxe Set Human IL-6, cat no.430504, Biolegend) was used. We observed that the amount of IL-6 expressed in M0 macrophages was lower than the detection range of conventional ELISA, as 2 different measurements from different samples matched 0 pg/ml, but IL-6 amount in those samples was detected using EliChip™ (Fig. 9A). For this reason, the amount of IL-6 was also assessed in the supernatant of M1 macrophages. Given the higher concentrations present in the sample, both techniques performed returned more precise values, still the quantification with EliChip™ was slightly increased (Fig. 9B).

EliChip™ performance brings to the *in vitro* diagnostics field: i. miniaturization of the assay allowing the target proteins concentration into small volumes; ii. immobilization of the antibody; iii. increased surface/volume ratio owing to 3D reaction chamber that improves the binding [108]; iv. elimination of TMB substrate contamination thanks to having a separated collection reservoir.

2.5.3. *EliChip™ analytical station: monitoring the healthy and OA-like model*

Once established and validated, we were able to use EliChip™ to perform the quantitative analysis of the engineered healthy and OA-like cartilage models. We checked the amount of IL-6 expressed by primary human chondrocytes of healthy construct and OA-like model at day 14 and day 28. IL-6, as an inflammatory cytokine, has been implicated one of the most abundantly expressed cytokine in the articular cartilage and synovial fluid in human OA [109,110]. IL-6 itself has no direct effect on the synthesis of proteolytic enzymes but it stimulates the MAPK signaling pathway and triggers signaling cascade activating catabolic reactions in joint and breaking cartilage homeostasis [111].

We observed almost 4 times higher IL-6 (mean: 3930 pg/ml) in OA-like model at day 14; and almost 3 times higher IL-6 (mean: 2180 pg/ml)

Table 3
Optimized intra-assay coefficient of variation (CV%) and inter-assay CV% values (IL-6, TNF-α and NGF) for EliChip™.

Analyte	Intra-Assay CV%	Inter-Assay CV%
IL-6	3.39 %	4.76 %
TNF-α	9.94 %	3.51 %
NGF	5.93 %	5.75 %

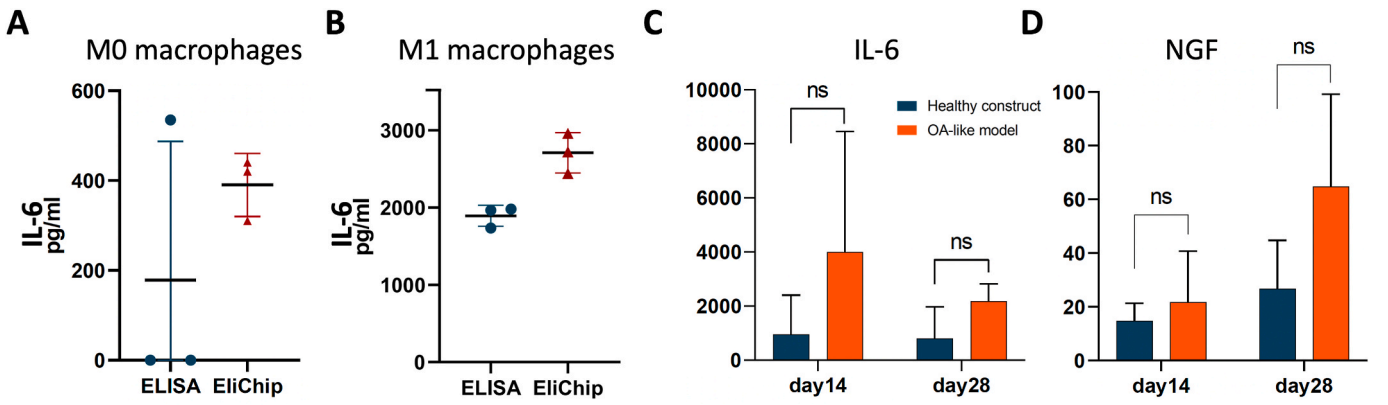

Fig. 9. Detection of IL-6 and NGF using EliChip™. Side-by side validation of EliChip™ compared to ELISA through detection of IL-6 from **A.** M0 macrophages **B.** M1 macrophages. **C.** Quantification of IL-6 produced by chondrocytes of healthy cartilage constructs (HC-S) and OA-like model at day 14 and day 28 using EliChip™. **D.** Quantification of NGF expressed by chondrocytes of HC-S and OA-like model at day 14 and day 28 using EliChip™. The statistical analysis was performed using Shapiro-Wilk test followed by Sidak's Multiple comparison test. The statistical significance level was set to $p < 0.05$; ns = non-significant. For each assay n = 3; 3 different donors.

at day 28 comparing to their respective time point healthy constructs (mean: 950 pg/ml at day14; 803 pg/ml at day 28 (Fig. 9C). These values prove that chondrocytes were producing IL-6 in response to inflammation since the detected amount of IL-6 from chondrocytes was 3 times higher at day 14 (mean: 3930 pg/ml) and 1.5 times higher at day 28 (mean: 2180 pg/ml), comparing the IL-6 coming from the M1 macrophage secretome. It should not be neglected that the secretome collected from macrophages was diluted with chondrogenic medium in 1:1 ratio, so the final concentration used to stimulate inflammation on chondrocytes is 1353 pg/ml. It should not also be ignored that even healthy chondrocytes can produce very low amounts of IL-6 (154.7 pg/ml), which is 3 times less than the amount expressed in OA human chondrocytes (427.9 pg/ml) [112].

We additionally performed quantification of NGF from HC-S (healthy construct) and OA-S (OA-like model) at day 14 and day 28, since NGF is a molecular target in the OA mice and human DRG in response to inflammation, and it can be involved as pain-inducing molecule owing to its role in mediating inflammatory pain [113,114]. The results showed that chondrocytes of OA-like model have tendency to produce higher NGF comparing to healthy construct chondrocytes both at day 14 and day 28 (Fig. 9D). Our finding is supported by Iannone et al. who showed that articular cartilage chondrocytes are expressing NGF mRNA through RT–PCR, and almost 41 % of the chondrocytes were defined NGF-positive cells through flow cytometry [115]. In line with this data, we hypothesized that axonal growth observed when sensory neurons exposed to OA-like model secretome (OA-S) might be implicated with the increased amount of NGF secreted by chondrocytes, considering NGF has been acknowledged as an essential growth factor for axonal guidance of sympathetic and sensory neurons in PNS [116]. Notably, in OA joints, NGF facilitates the nociceptor sensitivity and axonal terminal sprouting of SP+ and CGRP + sensory neurons in DRG through its receptor tropomyosin receptor kinase A (TrkA) [114,117–119]. Consequently, NGF stimulates a MAP kinase-signaling pathway which also has a role on both axonal outgrowth of sensory neurons [120], and inducing proinflammatory responses in human chondrocytes. These imbalances cause even more production of NGF and other inflammatory cytokines from chondrocyte, but the mechanism is yet to be identified [21,121]. Such bidirectional communication occurring between chondrocytes and sensory neurons is highly essential for controlling immune responses and nociception in the joint. Thus, having a technology as EliChip™ that allows the detection of growth factors, with impact on neuroimmune axis, from joint-on-chip models will favor the development of rationale insights of OA disease progression and mechanisms.

3. Conclusion

In this study, we successfully recapitulated the main hallmarks of human OA pathophysiology *in vitro*, through the implementation of OoC technology combined with highly sensitive quantitative analytical tools for microsystem monitoring. We delivered 3D engineered cartilage constructs, patterned inside microfluidic chips, presenting cartilage phenotypic markers and ECM production, stable for 28 days maturation.

By exposing the engineered constructs to the secretome of primary human proinflammatory macrophages, we successfully induced OA-like inflammatory responses, activating pathways that drive cartilage degradation. In parallel, we investigated the *in vitro* innervation profile of OA by assessing axonal growth in peripheral sensory neurons within the context of both healthy and inflamed 3D engineered cartilage models. This included analyzing paracrine effects mediated by the secretome as well as the bidirectional real-time crosstalk in coculture settings. Interestingly, we observed that sensory neurons exhibited enhanced axonal growth when exposed to the OA secretome alone; however, this effect was not replicated in direct coculture with the OA 3D engineered construct. These findings suggest that differences in local concentration and stability of key signaling factors, when sensory neurons and inflamed chondrocytes are in close proximity, might influence neuronal responses. Importantly, both the secretome and coculture approaches provide complementary insights into OA-model innervation mechanisms. The secretome assay allows for the study of soluble factors and their effects on sensory neurons, while the coculture model captures more complex cell-cell interactions within a shared environment. Together, these approaches offer a more comprehensive understanding of the mechanisms underlying OA-associated innervation and represent valuable tools for further exploration of OA pain pathways. Ultimately, we covered the need of microsystems quantitative analysis tools by providing reliable immune-based sensor technology - EliChip™ - to assess the molecular signature of cytokines and growth factors on both healthy and diseased models *in vitro*.

While this study advances joint-on-chip models and provides valuable insights into OA pathophysiology, certain limitations should be acknowledged. The available options for human sensory neurons remain limited, as protocols for deriving sensory neurons from human induced pluripotent stem cells (iPSCs) are still evolving. Recent advancements have shown promises, but current methods often face challenges, including variability in protocols and instability of sensory neurons phenotype over the maturation period. As a result, this study used mouse DRG sensory neurons, which, while sharing functional similarities with human sensory neurons, introduce interspecies differences in gene expression and pain signaling pathways that could influence the

outcomes observed. Future work could address this by incorporating human-derived sensory neurons as iPSC technology advances, reducing interspecies variation and enhancing the human relevance of the findings.

A key strength of this study is the use of patient-derived cells, such as chondrocytes and macrophages, which enhances the physiological relevance of the model. Incorporating cells directly from OA patients allows the system to more accurately reflect the unique characteristics of diseased joint tissues, making it possible to capture critical cellular behaviors and interactions that are representative of actual clinical conditions. By integrating these patient-specific cells into a microfluidic system, this model moves closer to replicating the complex environment of the osteoarthritic joint.

Despite current limitations in the availability of mature human sensory neuron models, this study marks an important step forward in simulating joint interactions and offers a valuable platform for exploring OA-associated pain mechanisms. The combination of OoC technology with highly sensitive immune-based sensors, capable of detecting OA-specific biomolecules within a single microfluidic device, has the potential to accelerate the discovery of molecular players involved in OA pathophysiology. This approach will also provide a more accurate system for drug testing and the development of new therapeutics for OA, bringing us closer to clinically relevant, personalized treatment options.

4. Experimental section

4.1. Hydrogel production and characterization

4.1.1. Preparation of the hydrogel

The hydrogel precursor solution (0.2 % w/v) lithium phenyl-2,4,6trimethylbenzoylphosphinate (LAP) (Sigma Aldrich, 90088) was prepared in prewarmed (50 °C) phosphate-buffered saline (PBS). Later, lyophilized GelMA (Cell ink, PhotoGel® 50 % DS) was dissolved in the precursor solution to a final concentration of 5 % or 10 % (w/v) at 50 °C and maintained at 37 °C. The cell/hydrogel solution at desired cell concentration and volume was prepared: i. 50 μl of 5M cell/ml concentration for each well of μ-Slide Angiogenesis (ibidi cat. no.81506); ii. 10 μl of 30M cells/ml for the channel of microfluidic device. The cell/hydrogel suspension was exposed to UV light at 365 nm at 10 mW/cm^2 power for 10 s. The crosslinked hydrogel constructs were cultured in differentiation media, defined below, at 37 °C for different time points for further analysis.

4.1.2. Porosity and swelling ratio of the hydrogel

The porosity of GelMA hydrogels was measured using the solvent replacement method (a technique based on the liquid absorption within the hydrogel) [40]. Crosslinked hydrogels were immersed in absolute ethanol and weighed at intervals (day 7, 14, 21, and 28) after removing the excess ethanol on the surface using filter paper. The porosity was calculated using the following formula:

$$\text{Porosity} = \left(\frac{W2 - W1}{\rho \text{V}}\right) \text{x } 100;$$

where W1 is the mass of the hydrogel before immersion in absolute ethanol, W2 is the mass of the hydrogel after immersion in absolute ethanol, ρ is the density of absolute ethanol, and V is the volume of the hydrogel. The swelling ratio of the hydrogel was evaluated by the weighing method [40]. The prepared samples were freeze-dried, and then the dry weight of the samples was recorded by an electronic balance (Mettler Toledo, AG285), followed by weighing of the hydrogels soaked in PBS buffer at intervals (day 7, 14, 21, and 28). The swelling ratio was calculated using the following formula:

$$\text{Swelling ratio} = \left(\frac{\textit{wet weight} - \textit{dry weight}}{\text{dry weight}}\right) \text{x } 100$$

4.1.3. Permeability and diffusion assay

To assess the diffusion capacity through GelMA hydrogel, the channel of the chondrocyte unit was prepared with two conditions: 1. The channel was fully-loaded with 5 % GelMA; 2. The patterns were formed in the channel using a high-resolution photomask (SELBA S.A., Fujifilm HPR7S) with black and transparent regions, the latter allowing selective passage of UV light. Afterwards, 3–5 kDa Fluorescein isothiocyanate (FITC)-dextran solution (0.5 mg/ml in PBS, Sigma-Aldrich, FD4) was added into the reservoirs and its diffusion through the hydrogel over time was monitored by fluorescence microscopy (equipment).

4.1.4. Mechanical properties

The rheological properties of GelMA hydrogel were measured by Kinexus Pro rheometer (Malvern Instruments, Malvern, UK) at 25 °C in a water-vapour saturated environment, immediately after preparation. GelMA hydrogels were crosslinked using the parameters previously defined, shaped as cylinder 8 mm diameter and 1.8 mm thickness, and incubated in PBS during the measurement. The linear viscoelastic region (LVR) of the samples was determined compressing the samples (oscillatory measurement gap) through amplitude sweep and frequency sweep measurements. The stress-strain graph was obtained using the amplitude sweep values at 20 % Strain, at 0.2Hz frequency (linear region). The corresponding Young's modulus was calculated from the curve of the stress-strain graph. All rheological measurements were made in triplicate.

4.1.5. Microfluidic design and fabrication

Both commercial (Xona Microfluidics, SND450) and home-fabricated microfluidic devices, containing similar features and dimensions, were used in the present study. The 2-compartment microfluidic device comprised two different unit (chondrocytes and nerve). Each unit included one central channel (1 mm width; 100 μm height) and 2 medium reservoirs (5 mm diameter), volume of 150 μl on each chamber. The two compartments of the device were connected through microgrooves (450 μm in length) to enable the separation of somal and axonal components of neuronal cells, reproducing the *in vivo* setting where only the neuronal projections reach the subchondral microenvironment. An adaptation for the nerve unit included neural cell chamber carved out using a 3 mm biopsy punch (no.BPP-30F, Kai Medical) for the seeding of dissociated sensory neurons.

To produce the devices in the lab, polydimethylsiloxane (PDMS, Sylgard® 184 Silicone Elastomer Kit; Down Corning) polymer mixture was prepared mixing thoroughly curing agent and base (1:10, w/w), degassed under vacuum, transferred into previously fabricated replica molds and polymerized at 70 °C for 1.5 h. Later, the cured PDMS plaque was cut, gently peeled from the mold. The medium reservoirs on both compartment of the device was formed using a 5 mm biopsy punch (no. BP-50F, Kai Medical) and a 3 mm punch (no.BPP-30F, Kai Medical) for seeding of dissociated sensory neurons. After sterilization of PDMS plaques and glass coverslips with 70 % ethanol, two layers were permanently bonded with O_2 plasma treatment for 10 s, creating hydroxyl groups on both surfaces for stable adhesive bonding and allowed to cure overnight at 70 °C before further experimental use, for hydrophobic recovery of the PDMS.

4.2. Cell culture

4.2.1. Ethics approval

Human chondrocytes: Human primary human chondrocytes were isolated from patients undergoing total joint replacement due to end-stage OA at the Centro Hospitalar Universitário de S.João, Portugal (ethical approval ref. 196/19). Written informed consent was received from all patients.

Primary human monocytes: Human monocytes were isolated from

buffy coats of healthy blood donors. These were kindly provided by the Immunohemotherapy Department of Centro Hospitalar São João (CHSJ) from Porto, Portugal. This is covered by the ethical approval of the service, under which blood donors give informed written consent for their blood byproducts to be used for research purposes (Protocol reference 90/19).

Mouse dorsal root ganglia: Animal experimental protocols comprising tissues and cell isolation were carried out with prior written approval of the constituted Institutional Animal Care and Use (Ethics) and the appropriate National Regulatory Authorities (DGV) in compliance with national (DL113/2013) and International (Directive 2010/63/EU) laws and policies (ORBEA 2018/34 and Direção-Geral de Alimentação e Veterinária (DGAV) 0421/000/000/2020). i3S facilities are licensed by DGAV and accredited by AAALAC and follow Federation of European Laboratory Animal Science Associations (FELASA) guidelines and recommendations regarding laboratory animal welfare. EN holds accreditation as Research-Coordinator for animal experiments (2008, C category, FELASA). All animal procedures were approved by the i3S ethics committee and by the Portuguese Agency for Animal Welfare (DGAV) in accordance with the EU Directive (2010/63/EU) and Portuguese law (DL 113/2013). Mice were housed at 22 °C with a 12 h light/dark cycle with ad libitum access to water and food.

4.2.2. Primary human chondrocytes isolation and culture

Human primary chondrocytes were isolated from patients. Firstly, healthy looking cartilage tissue (distal and/or posterior femoral condyles) was dissected from the joint and transferred into the isolation medium (low glucose Dulbecco's modified eagles' medium (DMEM) (Gibco 21885), 5 % Penicillin/Streptomycin (Pen/Strep) (Gibco 15140122), 5 % Fungizone (Biowest, L0009) while the dissection is completed. The cartilage tissues were digested in digestion medium (DMEM, High Glucose, (Gibco 31966-021); 5 % FBS and 0,15 % Collagenase B (Roche, 11 088 815 001)) for overnight at 37 °C with agitation. The cells were passed through a 100 μm cell strainer and centrifuged at 1200 rpm for 12 min; the pellet was resuspended in DMEM high glucose (Gibco 31966-021) supplemented with 10 % FBS (Biowest, S181B-50), 100 U/mL penicillin G, and cells were counted. Cells were expanded in T75flasks in a humidified atmosphere with 5 % CO_2 at 37 °C, in expansion medium (DMEM high glucose + 1 % Pen/Strep (Gibco 15140122), +1 % HEPES 1M (Gibco, 15630080) + Sodium Pyruvate 1 mM (Gibco, 11360070) + 5 ng/ml bFGF (Sigma Aldrich, 0291) + 1 ng/mL TGF-β1 (R&D, 100-B-001)) until confluency. The experiments were performed with the cells between passages 1 and 4.

4.2.3. Primary human monocyte isolation and differentiation

Primary human monocytes were isolated from buffy coats of healthy blood donors. Briefly, blood was centrifuged at 1200 g, with acceleration 5 and no brake for 20 min at room temperature (RT) to collect the PBMC layer, taking advantage of the density gradient. PBMCs were incubated with the RosetteSep (StemCell Technologies, 15068) (67 μL of RosetteSep/1 ml of PBMC) for 20 min on a roller agitator at RT, and diluted in an equal volume of 2 % FBS: PBS mix. Later, the mix (PBMCs + PBS+2%FBS) was transferred gently to the top of a Ficoll-Histopaque (Sigma-Aldrich, 10771) layer with half the volume of the mix, centrifuged at 1200 g for 20 min at RT to collect the interphase cell layer with a Pasteur pipette. The interphase layer was washed 3 times with PBS 1X and centrifuged at 1300 rpm for 6 min at RT. The final pellet was resuspended in RPMI culture medium (RPMI 1640 Medium GlutaMax, Gibco, 61870-010; FBS, Biowest, S181BH; 5 % Pen/Strep (Gibco 15140122), 500K cells were seeded on sterile coverslips 15 mmØ in 24-well plate and cultured with 50 ng/ml M-CSF (ImmunoTools, 11343115) for 7 days at 37 °C. Later, the monocytes were incubated in the culture medium without M-CSF for 3 days before the stimulation. Monocytes were treated with 10 ng/ml LPS and 50 ng/ml IFN-γ for 72 h to polarize towards an M1 phenotype. After the polarization, M1 macrophage secretome was collected and stored at −80 °C for further use to develop inflamed cartilage construct and for further analysis (ELISA, EliChip™ analysis), while the cells were used for flow cytometric analysis.

4.2.4. Primary mouse dorsal root ganglion isolation, dissociation and culture

Dorsal root ganglia (DRG) were isolated from the spinal cord of C57BL/6 mice mouse embryos (E16.5). DRG were maintained in Hank's balanced salt solution (HBSS, Sigma Aldrich H9269) until the isolation was completed. For biocompatibility test, DRG explants were cultured on 5 and 10 % GelMA, prepared as previously defined, for 4 days. For the microfluidic culture, enzymatic dissociation of DRG was performed in two steps. First, DRG were incubated with 0.1 % collagenase type IV (Sigma, C5138) in HBSS for 30 min at 37 °C. Later, cells were incubated with Trypsin EDTA 0.125 % (Gibco, 25200056) at the final ratio of 1:1 (Trypsin EDTA 0.125 %: Col-IV: HBSS mix) for 15 min at 37 °C. Proteolytic enzymes were blocked through 10 % FBS addition and mechanical dissociation was performed by pipetting up and down. Later, cells were centrifuged at 1500 rpm for 5 min and one more mechanical dissociation step was performed in HBSS, followed by centrifugation. Finally, cells were resuspended in Neurobasal plus medium (Gibco, A3582901) supplemented with 2 % v/v B-27 Serum-Free Supplements (B-27, Invitrogen, LTI17504-044), 60 mM 5-fluoro-20-deoxyuridine (FDU, Sigma-Aldrich, 46875), 25 mM Glucose (Glu, Sigma-Aldrich, G6152), 1 mM Sodium pyruvate (Gibco, 11360-039), 50 ng/ml Nerve Growth Factor (NGF, Merck, 480354), 2 mM Glutamax (Gibco, 35050061) and 1 % Pen/Strep. Finally, embryonic sensory neurons were plated in the nerve unit of the microfluidic devices at a density of 10M cells/5 μl per chip.

4.2.5. Healthy tissue engineered construct development, in-chip

After expansion, human articular chondrocytes were detached using 0.25 % Trypsin and centrifuged at 1200 rpm for 5 min. Afterwards, the cells were resuspended in desired volume of 5 % GelMA solution at 37 °C, as previously described. The channel of chondrocyte unit of the device was slowly filled with 10 μl of cell/hydrogel solution through medium reservoirs, avoiding leaking of the hydrogel towards microgrooves, covered with the photomask from the coverslip side, the hydrogel was crosslinked using previously defined parameters. Non-crosslinked GelMA was removed from the channel washing with pre-warmed PBS 1X. For the first 4 h, the cartilage tissue construct was maintained with 20 μl of chondrogenic medium in each medium reservoir to avoid fluidic movement on the cells. Later, the construct was cultured adding 30 μl of differentiation medium at 37 °C until the further experimental analysis on day 7, day 14 and day 28. The culture medium was gently changed by manual pipetting every other day. Differentiation medium (DMEM high glucose, Gibco 31966-021), supplemented with 0.17 mM L-ascorbic acid 2-phosphate (Sigma Aldrich), 0.1 μM dexamethasone (Sigma Aldrich), 100 units/ml penicillin and 100 mg/ml streptomycin, and 10 ng/ml TGF-β3 (R&D Systems), 5 μg/ml of insulin (Sigma), 5 μg/ml of transferrin (Sigma), 5 ng/ml of selenium acid (Sigma), 1 mM of sodium pyruvate (Gibco), 0.35 mM of proline (Sigma), 1.25 mg/ml of bovine serum albumin (BSA, Sigma).

4.2.6. Inflamed 3D engineered cartilage construct development, in-chip

The inflamed tissue engineered construct was developed exposing the healthy cartilage construct to the biochemical stimulation. To create the inflammatory environment, differentiation medium/M1 macrophage secretome (1:1) mix was prepared. The healthy construct was subjected to inflammatory environment for 48 h before the end of time points (day 14 and day 28).

Secretome assay: Prior to the seeding of embryonic sensory neurons, the microfluidic chambers were assembled on previously PDL coated (100 μg/mL, Sigma Aldrich, P7280) coverslips according to manufacturer's guide. Later, the chips were coated with 5 μg/mL laminin (Sigma Aldrich, L2020), prepared in previously defined Neurobasal plus

medium, and incubated overnight at 37 °C. After removal of laminin coating, embryonic sensory neurons were seeded in the nerve unit (somal) of the microfluidic device at previously defined density in presence of 3D engineered cartilage constructs secretome which was collected at day 28, once the chondrogenic differentiation was achieved. The conditions assessed are: chondrogenic medium (CM; not in contact with any chondrocytes) as a control to healthy construct secretome (HC-S), macrophage secretome mix (MS) (1:1, chondrogenic medium and M1 macrophage secretome) as a control to inflamed construct secretome (OA-S) as described in Table 1. The culture was maintained for 5 days. The culture medium of sensory neurons was gently refreshed once throughout the culture time.

4.2.7. Coculturing of 3D engineered cartilage constructs with sensory neurons

The healthy cartilage construct (HCC) was developed as previously defined above. When the HCC reached day 7, the inflamed tissue engineered construct was induced by exposing the HCC into proinflammatory environment for 48 h, also defined above. When both HCC and inflamed construct reached at day 9, dissociated primary sensory neurons (at a density of 10M cells/5 μl per chip) were seeded in the nerve unit of the 2-compartment microfluidic device, previously coated with laminin. The coculture was maintained for 5 days in their cell-specific culture media. The culture medium for sensory neurons and human chondrocytes were gently refreshed every other day.

4.3. Cell culture assays

4.3.1. Live/dead assay

Cell viability was assessed through Calcein and propidium iodide (PI) staining of chondrocytes encapsulated in i. 5 % GelMA and 10 % GelMA in ibidi μ-Slide Angiogenesis slide (cat. no.81506); ii. patterned chondrocytes inside the microfluidic device for healthy and inflamed cartilage construct. In both cases, after removal of culture medium, cells were washed with PBS 1X and incubated with 3 μM Calcein-AM for 30 min protecting from light. Followed by another washing step with 1X PBS and incubation with 2,5 μM PI for 3 min. As positive control for PI, cells were fixed with 4 % PFA and stained only with 2,5 μM PI for 3 min. Stained samples were imaged using a confocal laser scanning microscopy (Leica SP5 for ibidi μ-Slide Angiogenesis slide; Leica SP8 for microfluidic culture). Confocal Z-stack projections were processed with Fiji-ImageJ version 2.9.0/1.53t.

4.3.2. Metabolic activity

To study the metabolic changes during chondrogenic differentiation, cells were cultured with chondrogenic medium for 7 days outside the microfluidic device. For the metabolic assay, resazurin solution (0.1 mg/ml) was added to each well of the ibidi μ-Slide Angiogenesis slide (cat. no.81506) with 10 % (v/v = resazurin/culture medium) and incubated for 4 h at 37 °C. Fluorescence of resorufin (reduced product of resazurin by metabolically active cell) is measured at 530 nm for excitation, 590 nm for emission. Cell metabolic activity was calculated according to the formula below:

$$\text{Cell metabolic activity } (\%) = 100 \times \frac{\textit{Experimental Resofurin release } (530ex; 590em)}{\textit{Maximum Resofurin release; control group } (530ex; 590em)}$$

4.3.3. Fluorescence-activated cell sorting (FACS)

To evaluate the expression differences of cytokine receptors between the M0 macrophages and proinflammatory M1 macrophages, FACS analysis was performed after the cells were stimulated with 10 ng/ml of LPS and 50 ng/ml INF-y for 72 h. Briefly, the cells were harvested and rinsed with PBS. Cell suspensions were incubated with antihuman CD14-FTIC (BioLegend, 301804), CD86 - PE-Cy7 (BioLegend, 305422) and HLA-DR-BV42 (BioLegend, 307636) antibodies at 4 °C for 20 min. Cells were then rinsed with PBS and analyzed by flow cytometry (Beckman Coulter, U.S.A). The data were analyzed via FlowJo software version 10.8.2 (BD Biosciences).

4.3.4. Enzyme-linked immunosorbent assay (ELISA)

Polarization of primary human monocytes into M1 Proinflammatory macrophages was confirmed by ELISA for IL-6, IL-1β and TNF-α (Human IL-6, ELISA MAX, Deluxe Set, 430504; Human IL-1β, ELISA MAX, Deluxe Set, 437004; Human TNF-α, ELISA MAX, Deluxe Set, 430204). Assays were performed according to manufacturer's instructions.

4.3.5. Alcian blue staining

After the fixation of cells with 4 % PFA, cells were washed with PBS extensively and stained with Alcian blue reagent solution for 30 min. Proteoglycans were observed under a bright field microscope (equipment).

4.3.6. Immunofluorescence staining and confocal analysis

After the establishment of healthy and OA-like models, chondrocytes were fixed with 4 % v/v PFA and sensory neurons were fixed with 4 % v/v PFA and 4 % v/v sucrose (Duchefa Biochemie, S0809) mix for 20 min at RT. Primary antibodies were diluted in blocking buffer (5 % FBS in 0.25 % triton X) and added to samples overnight at 4 °C. Primary antibodies were used: beta-III tubulin (1:2000, G7121; Promega); Col-II (1:100, ab34712, Abcam); ACAN (1:50, 13880-1-AP, Proteintech Europe); SOX9 (1:100, NBP2-24659, Bio-Techne); MMP13 (1:100, ab39012; Abcam); Col-X (1:100, ab49945, Abcam). After washing samples in PBS three times, they were incubated for 1 h at RT with the respective secondary antibodies (1:1000 AlexaFluor 488 donkey anti-mouse (A11057, Invitrogen), AlexaFluor 568 goat anti-rabbit (A11011, Invitrogen) or AlexaFluor 647 goat anti-mouse (A21235, Invitrogen). For actin staining samples were incubated for 1h RT with AlexaFluor™ 488 Phalloidin (1:100). Samples were then washed with PBS and counterstained with 4′,6-diamidino-2- phenylindole (DAPI) (1:10 000 in PBS) for 10 min at RT. Samples were imaged using a confocal laser scanning microscopy (Leica SP8). Confocal Z-stack projections were acquired and processed with Fiji-ImageJ.

4.3.7. Quantification of Col-II, MMP13 and Col-X proteins

Following the staining of the 3D engineered constructs with Col-II, MMP13 and Col-X, as described above, confocal z-stack projections of a single patterns within the channels were acquired. To calculate the intensity of the signal within the chondrocyte pattern, at first, each pattern's size was manually determined to guarantee the proper stained area and prevent the entire image from being used as an area setting. Later, using the measure command of the Fiji, integrated density (IntDen) was calculated the full z-stack image. Measured IntDen then was divided to defined and measured pattern area to obtain Intensity/Area measurements.

4.3.8. Quantitative reverse transcriptase polymerase chain reaction (qRT-PCR) analysis

Prior RNA extraction, 3D engineered constructs (3–5 chips per condition) were incubated with 2 mg/mL collagenase B (#11088831001, Roche) for 30 min at 37 °C. Cells were collected from the microfluidic chips into an RNAse-free tube and centrifuged for 5 min at 300g. NR buffer containing 1 % of β-mercaptoethanol was added to the cell pellet. Samples were stored at −20 °C for later extraction. Total RNA was extracted using the NZY Total RNA Isolation Kit (MB13402, NZYtech) according to the manufacturer's protocol. RNA final concentration and purity (OD260/280) were determined using a NanoDrop 2000 instrument (NanoDrop Technologies). RNA was reverse transcribed into cDNA using the NZY First-Strand cDNA Synthesis Kit (NZYTech), according to the manufacturer's protocol. For the analysis of repulsive cues, a personalized PrimePCR array (Bio-Rad Laboratories) was performed. qRT-PCR experiments were run using the PCR CFX384 thermal cycler

(Bio-Rad Laboratories) and analyzed with the CFX manager software (Bio-Rad Laboratories). Target gene expression was quantified using the cycle threshold (Ct) values and relative mRNA expression levels were calculated as follows: 2^(Ct reference gene − Ct target gene). Human actin β was used as a reference gene. Both target and reference genes were amplified with efficiencies between 100 % ± 5 %.

4.3.9. Axonal outgrowth

DRG were fixed and stained with beta-III tubulin as described above. Images were acquired with confocal laser scanning microscopy (Leica SP8). Axonal outgrowth of DRG was quantified using Outgrowth Analytics (MATLAB) for the DRG cultured on 5 and 10 % GelMA for 4 days; and using AxoFluidic for the microfluidic culture as previously described [59].

4.4. Quantitative monitoring of engineered microtissue in the microfluidic platform

4.4.1. Fabrication of Elichip™ LoCs

18 reaction chamber LoCs and the reading LoCs were fabricated by computer numerical control (CNC) milling in poly methyl methacrylate (PMMA) and thermally bonded. Reaction LoCs are disposable as conventional ELISA plate.

4.4.2. IL-6 and NGF quantification using EliChip™

Quantification of IL-6 and NGF was performed based on the enzymatic immunoassay and antibody-antigen affinity. For the detection of both IL-6 and NGF, the protocol has been settled as a sandwich ELISA with a capture antibody (IL-6 Monoclonal Antibody (MQ2-13A5), eBioscience; Purified anti-human NGF Antibody, 509601, Biolegend) coated in the reaction chamber and their respective biotinylated detection antibodies (IL-6 Monoclonal Antibody (MQ2-39C3), Biotin, eBioscience; Biotin anti-mouse/human NGF Antibody, 509801, Biolegend). The target molecule is bound by the antibody pair to two different epitopes and the biotin is bound by streptavidin conjugated with Horseradish Peroxidase (HRP) enzyme (ThermoFisher, N200). TMB (ThermoFisher, 34028) is used as a colorimetric substrate. 3,3′,5,5′ tetramethylbenzidine (TMB) oxidizes in the presence of HRP and turns blue directly proportional to the target molecule concentration. The oxidation reaction is stopped by adding HCl, 1M and the optical density is measured at 450 nm. The unknown concentration has been calculated through linear regression on a standard calibration curve. Volume of all the reagents and samples loaded to the reaction chamber was 20 μl. The same protocol was used to establish the TNF-α detection protocol, using TNF-alpha standard solution (Human TNF-α Recombinant Protein, Invitrogen, from ThermoFisher) diluted in PBS-BSA 0.1 % dilution buffer at different concentrations prepared before use. A monoclonal capture antibody (TNF-α Monoclonal Antibody (MAb1), eBioscience™ from ThermoFisher) was selected to maximize the selectivity of the antigen and improve the assay's overall sensibility. It was used in pair with a biotinylated monoclonal antibody (TNF-α Monoclonal Antibody (MAb11), Biotin, eBioscience™ from ThermoFisher).

4.4.3. Statistical analysis

All experiments were repeated at least three times. In all experiments, data sets were subjected to the Shapiro-Wilk test homogeneity of variance test to assess if they followed a normal distribution. For data following normal distribution parametric one-way ANOVA followed by Tukey's multiple comparisons test; or unpaired *t*-test was performed, while no normal distributions were analyzed using non-parametric Kruskal-Wallis statistic followed by Dunn's multiple comparisons test; or Mann-Whitney tests to assess statistically significant differences. Differences between groups were considered statistically significant when *p < 0.05, **p < 0.01, ***p < 0.001, ****p < 0.0001. Data analysis was performed using GraphPad Prism software (10.1.1 (270).

CRediT authorship contribution statement

Emine Kahraman: Writing – review & editing, Writing – original draft, Visualization, Validation, Methodology, Investigation, Formal analysis, Data curation. **Daniela Vasconcelos:** Writing – review & editing, Resources, Investigation. **Beatriz Ribeiro:** Resources, Investigation. **Ana Carolina Monteiro:** Resources, Investigation. **Enzo Mastromatteo:** Validation, Methodology. **Andrea Bortolin:** Methodology, Investigation. **Marina Couto:** Resources, Investigation. **Laura Boschis:** Resources, Project administration. **Meriem Lamghari:** Supervision, Project administration, Funding acquisition, Conceptualization. **Estrela Neto:** Writing – review & editing, Validation, Supervision, Project administration, Methodology, Conceptualization.

Declaration of generative AI and AI-assisted technologies in the writing process

During the preparation of this work the authors used ChatGPT in the writing process to improve the readability and language of the manuscript. After using this tool, the authors reviewed and edited the content as needed and take(s) full responsibility for the content of the publication.

Declaration of competing interest

The authors declare the following financial interests/personal relationships which may be considered as potential competing interests: Laura Boschis has patent #102016000077085 issued to Assignee. Laura Boschis has patent #102017000083692 issued to Assignee. Laura Boschis has patent #17751483.3 pending to Assignee. If there are other authors, they declare that they have no known competing financial interests or personal relationships that could have appeared to influence the work reported in this paper.

Acknowledgments

This work has received funding from the European Union's Horizon 2020 research and innovation program under grant agreement No. 860462 and No. 953121. DV, MC, ACM and EN received funding from Fundação para a Ciência e Tecnologia - FCT (2021.03374.CEECIND; 2020.05177.BD; 2021.07775.BD; CEECIND/01760/2018, respectively).

The authors acknowledge the support of i3S Scientific Platform Advanced Light Microscopy and Bioimaging, members of the national infrastructure PPBI-Portuguese Platform of BioImaging (POCI-01-0145-FEDER-022122), Translational Cytometry unit, and Histology and Electron Microscopy facilities at i3S.

The authors acknowledge Ricardo Vidal for their technical assistance on mechanical tests, Ruben Pereira for providing equipment for hydrogels production.

Appendix A. Supplementary data

Supplementary data to this article can be found online at https://doi.org/10.1016/j.mtbio.2025.101491.

Data availability

Data will be made available on request.

References

[1] J.D. Steinmetz, G.T. Culbreth, L.M. Haile, Q. Rafferty, J. Lo, K.G. Fukutaki, J. A. Cruz, A.E. Smith, S.E. Vollset, P.M. Brooks, M. Cross, A.D. Woolf, H. Hagins, M. Abbasi-Kangevari, A. Abedi, I.N. Ackerman, H. Amu, B. Antony, J. Arabloo, A. Y. Aravkin, A.M. Argaw, A.A. Artamonov, T. Ashraf, A. Barrow, L.M. Bearne, I. M. Bensenor, A.Y. Berhie, N. Bhardwaj, P. Bhardwaj, V.S. Bhojaraja, A. Bijani, P. S. Briant, A.M. Briggs, N.S. Butt, J. Charan, V.K. Chattu, F.M. Cicuttini,

K. Coberly, O. Dadras, X. Dai, L. Dandona, R. Dandona, K. de Luca, E. Denova-Gutiérrez, S.D. Dharmaratne, M. Dhimal, M. Dianatinasab, K.E. Dreinhoefer, M. Elhadi, U. Farooque, H.R. Farpour, I. Filip, F. Fischer, M. Freitas, B. Ganesan, B.N.B. Gemeda, T. Getachew, S.-H. Ghamari, A. Ghashghaee, T.K. Gill, M. Golechha, D. Golinelli, B. Gupta, V.B. Gupta, V.K. Gupta, R. Haddadi, N. Hafezi-Nejad, R. Halwani, S. Hamidi, A. Hanif, N.I. Harlianto, J.M. Haro, J. Hartvigsen, S.I. Hay, J.J. Hebert, G. Heidari, M.-S. Hosseini, M. Hosseinzadeh, A.K. Hsiao, I.M. Ilic, M.D. Ilic, L. Jacob, R. Jayawardena, R.P. Jha, J.B. Jonas, N. Joseph, H. Kandel, I.M. Karaye, M.J. Khan, Y.J. Kim, A.-A. Kolahi, O. Korzh, R. Koteeswaran, V. Krishnamoorthy, G.A. Kumar, N. Kumar, S.-w. Lee, S.S. Lim, S.W. Lobo, G. Lucchetti, M.-R. Malekpour, A.A. Malik, L.G.G. Mandarano-Filho, S. Martini, A.-F.A. Mentis, M.K. Mesregah, T. Mestrovic, E.M. Mirrakhimov, A. Misganaw, R. Mohammadpourhodki, A.H. Mokdad, S. Momtazmanesh, S. D. Morrison, C.J.L. Murray, H. Nassereldine, H.B. Netsere, S. Neupane Kandel, M. O. Owolabi, S. Panda-Jonas, A. Pandey, S. Pawar, P. Pedersini, J. Pereira, A. Radfar, M.-M. Rashidi, D.L. Rawaf, S. Rawaf, R. Rawassizadeh, S.-M. Rayegani, D. Ribeiro, L. Roever, B. Saddik, A. Sahebkar, S. Salehi, L. Sanchez Riera, F. Sanmarchi, M.M. Santric-Milicevic, S. Shahabi, M.A. Shaikh, E. Shaker, M. Shannawaz, R. Sharma, S. Sharma, J.K. Shetty, R. Shiri, P. Shobeiri, D.A. S. Silva, A. Singh, J.A. Singh, S. Singh, S.T. Skou, H. Slater, M.S. Soltani-Zangbar, A.V. Starodubova, A. Tehrani-Banihashemi, S. Valadan Tahbaz, P.R. Valdez, B. Vo, L.G. Vu, Y.-P. Wang, S.H. Yahyazadeh Jabbari, N. Yonemoto, I. Yunusa, L. M. March, K.L. Ong, T. Vos, J.A. Kopec, Global, regional, and national burden of osteoarthritis, 1990–2020 and projections to 2050: a systematic analysis for the Global Burden of Disease Study 2021, The Lancet Rheumatology 5 (9) (2023) e508–e522.

[2] S. Grässel, The role of peripheral nerve fibers and their neurotransmitters in cartilage and bone physiology and pathophysiology, Arthritis Res. Ther. 16 (6) (2014) 485.

[3] Y. Chen, B. Zhao, Y. Zhu, H. Zhao, C. Ma, HIF-1-VEGF-Notch mediates angiogenesis in temporomandibular joint osteoarthritis, Am J Transl Res 11 (5) (2019) 2969–2982.

[4] S. Suri, S.E. Gill, S. Massena de Camin, D. Wilson, D.F. McWilliams, D.A. Walsh, Neurovascular invasion at the osteochondral junction and in osteophytes in osteoarthritis, Ann. Rheum. Dis. 66 (11) (2007) 1423–1428.

[5] H.J. Samvelyan, D. Hughes, C. Stevens, K.A. Staines, Models of osteoarthritis: relevance and new insights, Calcif. Tissue Int. 109 (3) (2021) 243–256.

[6] N. Picollet-D'hahan, A. Zuchowska, I. Lemeunier, S. Le Gac, Multiorgan-on-a-Chip: a systemic approach to model and decipher inter-organ communication, Trends Biotechnol. 39 (8) (2021) 788–810.

[7] M. Rothbauer, H. Zirath, P. Ertl, Recent advances in microfluidic technologies for cell-to-cell interaction studies, Lab Chip 18 (2) (2018) 249–270.

[8] Q. Wu, J. Liu, X. Wang, L. Feng, J. Wu, X. Zhu, W. Wen, X. Gong, Organ-on-a-chip: recent breakthroughs and future prospects, Biomed. Eng. Online 19 (1) (2020) 9.

[9] E. Kahraman, R. Ribeiro, M. Lamghari, E. Neto, Cutting-edge technologies for inflamed joints on chip: how close are we? Front. Immunol. 13 (2022).

[10] Z.A. Li, S. Sant, S.K. Cho, S.B. Goodman, B.A. Bunnell, R.S. Tuan, M.S. Gold, H. Lin, Synovial joint-on-a-chip for modeling arthritis: progress, pitfalls, and potential, Trends Biotechnol. 41 (4) (2023) 511–527.

[11] C. Mondadori, S. Palombella, S. Salehi, G. Talò, R. Visone, M. Rasponi, A. Redaelli, V. Sansone, M. Moretti, S. Lopa, Recapitulating monocyte extravasation to the synovium in an organotypic microfluidic model of the articular joint, Biofabrication 13 (4) (2021) 045001.

[12] P. Occhetta, A. Mainardi, E. Votta, Q. Vallmajo-Martin, M. Ehrbar, I. Martin, A. Barbero, M. Rasponi, Hyperphysiological compression of articular cartilage induces an osteoarthritic phenotype in a cartilage-on-a-chip model, Nat. Biomed. Eng. 3 (7) (2019) 545–557.

[13] C.A. Paggi, J. Hendriks, M. Karperien, S. Le Gac, Emulating the chondrocyte microenvironment using multi-directional mechanical stimulation in a cartilage-on-chip, Lab Chip 22 (9) (2022) 1815–1828.

[14] C.A. Paggi, B. Venzac, M. Karperien, J.C.H. Leijten, S. Le Gac, Monolithic microfluidic platform for exerting gradients of compression on cell-laden hydrogels, and application to a model of the articular cartilage, Sensor. Actuator. B Chem. 315 (2020) 127917.

[15] S. Piluso, Y. Li, F. Abinzano, R. Levato, L. Moreira Teixeira, M. Karperien, J. Leijten, R. van Weeren, J. Malda, Mimicking the articular joint with in vitro models, Trends Biotechnol. 37 (10) (2019) 1063–1077.

[16] J. Rosser, B. Bachmann, C. Jordan, I. Ribitsch, E. Haltmayer, S. Gueltekin, S. Junttila, B. Galik, A. Gyenesei, B. Haddadi, M. Harasek, M. Egerbacher, P. Ertl, F. Jenner, Microfluidic nutrient gradient–based three-dimensional chondrocyte culture-on-a-chip as an in vitro equine arthritis model, Materials Today Bio 4 (2019) 100023.

[17] M. Rothbauer, R.A. Byrne, S. Schobesberger, I. Olmos Calvo, A. Fischer, E. I. Reihs, S. Spitz, B. Bachmann, F. Sevelda, J. Holinka, W. Holnthoner, H. Redl, S. Toegel, R. Windhager, H.P. Kiener, P. Ertl, Establishment of a human three-dimensional chip-based chondro-synovial coculture joint model for reciprocal cross talk studies in arthritis research, Lab Chip 21 (2021) 4128–4143.

[18] S. Salehi, S. Brambilla, M. Rasponi, S. Lopa, M. Moretti, Development of a microfluidic vascularized osteochondral model as a drug testing platform for osteoarthritis, Adv. Healthcare Mater. (2024) e2402350.

[19] S. Grässel, D. Muschter, Peripheral nerve fibers and their neurotransmitters in osteoarthritis pathology, Int. J. Mol. Sci. 18 (5) (2017) 931.

[20] C. Mondadori, S. Palombella, S. Salehi, G. Talò, R. Visone, M. Rasponi, A. Redaelli, V. Sansone, M. Moretti, S. Lopa, Recapitulating monocyte extravasation to the synovium in an organotypic microfluidic model of the articular joint, Biofabrication 13 (4) (2021).

[21] T.L. Vincent, Peripheral pain mechanisms in osteoarthritis, Pain 161 (2020).

[22] C.L. Thompson, S. Fu, H.K. Heywood, M.M. Knight, S.D. Thorpe, Mechanical stimulation: a crucial element of organ-on-chip models, Front. Bioeng. Biotechnol. 8 (2020).

[23] G.A. Clarke, B.X. Hartse, A.E. Niaraki Asli, M. Taghavimehr, N. Hashemi, M. Abbasi Shirsavar, R. Montazami, N. Alimoradi, V. Nasirian, L.J. Ouedraogo, N. N. Hashemi, Advancement of sensor integrated organ-on-chip devices, Sensors 21 (4) (2021) 1367.

[24] A. Hasan, M. Nurunnabi, M. Morshed, A. Paul, A. Polini, T. Kuila, M. Al Hariri, Y. K. Lee, A.A. Jaffa, Recent advances in application of biosensors in tissue engineering, BioMed Res. Int. 2014 (2014) 307519.

[25] T. Kilic, F. Navaee, F. Stradolini, P. Renaud, S. Carrara, Organs-on-chip monitoring: sensors and other strategies, Microphysiological Systems 2 (2018).

[26] J.A. Stenken, A.J. Poschenrieder, Bioanalytical chemistry of cytokines–a review, Anal. Chim. Acta 853 (2015) 95–115.

[27] J.U. Lind, T.A. Busbee, A.D. Valentine, F.S. Pasqualini, H. Yuan, M. Yadid, S.-J. Park, A. Kotikian, A.P. Nesmith, P.H. Campbell, J.J. Vlassak, J.A. Lewis, K. K. Parker, Instrumented cardiac microphysiological devices via multimaterial three-dimensional printing, Nat. Mater. 16 (3) (2017) 303–308.

[28] M.A. Ortega, X. Fernández-Garibay, A.G. Castaño, F. De Chiara, A. Hernández-Albors, J. Balaguer-Trias, J. Ramón-Azcón, Muscle-on-a-chip with an on-site multiplexed biosensing system for in situ monitoring of secreted IL-6 and TNF-α, Lab Chip 19 (15) (2019) 2568–2580.

[29] H.V. Almeida, R. Eswaramoorthy, G.M. Cunniffe, C.T. Buckley, F.J. O'Brien, D. J. Kelly, Fibrin hydrogels functionalized with cartilage extracellular matrix and incorporating freshly isolated stromal cells as an injectable for cartilage regeneration, Acta Biomater. 36 (2016) 55–62.

[30] K. Markstedt, A. Mantas, I. Tournier, H. Martínez Ávila, D. Hägg, P. Gatenholm, 3D bioprinting human chondrocytes with nanocellulose-alginate bioink for cartilage tissue engineering applications, Biomacromolecules 16 (5) (2015) 1489–1496.

[31] Y.P. Singh, A. Bandyopadhyay, B.B. Mandal, 3D bioprinting using cross-linker-free silk–gelatin bioink for cartilage tissue engineering, ACS Appl. Mater. Interfaces 11 (37) (2019) 33684–33696.

[32] C.-C. Wang, K.-C. Yang, K.-H. Lin, Y.-L. Liu, H.-C. Liu, F.-H. Lin, Cartilage regeneration in SCID mice using a highly organized three-dimensional alginate scaffold, Biomaterials 33 (1) (2012) 120–127.

[33] P. Yeung, K.H. Cheng, C.H. Yan, B.P. Chan, Collagen microsphere based 3D culture system for human osteoarthritis chondrocytes (hOACs), Sci. Rep. 9 (1) (2019) 12453.

[34] X. Zhan, Effect of matrix stiffness and adhesion ligand density on chondrogenic differentiation of mesenchymal stem cells, J. Biomed. Mater. Res. 108 (3) (2020) 675–683.

[35] I. Pepelanova, K. Kruppa, T. Scheper, A. Lavrentieva, Gelatin-Methacryloyl (GelMA) hydrogels with defined degree of functionalization as a versatile toolkit for 3D cell culture and extrusion bioprinting, Bioengineering 5 (3) (2018) 55.

[36] W. Schuurman, P.A. Levett, M.W. Pot, P.R. van Weeren, W.J. Dhert, D. W. Hutmacher, F.P. Melchels, T.J. Klein, J. Malda, Gelatin-methacrylamide hydrogels as potential biomaterials for fabrication of tissue-engineered cartilage constructs, Macromol. Biosci. 13 (5) (2013) 551–561.

[37] M.Y. Shie, J.J. Lee, C.C. Ho, S.Y. Yen, H.Y. Ng, Y.W. Chen, Effects of gelatin methacrylate bio-ink concentration on mechano-physical properties and human dermal fibroblast behavior, Polymers 12 (9) (2020).

[38] J. Visser, D. Gawlitta, K.E. Benders, S.M. Toma, B. Pouran, P.R. van Weeren, W. J. Dhert, J. Malda, Endochondral bone formation in gelatin methacrylamide hydrogel with embedded cartilage-derived matrix particles, Biomaterials 37 (2015) 174–182.

[39] Y. Wang, M. Ma, J. Wang, W. Zhang, W. Lu, Y. Gao, B. Zhang, Y. Guo, Development of a photo-crosslinking, biodegradable GelMA/PEGDA hydrogel for guided bone regeneration materials, Materials 11 (8) (2018) 1345.

[40] S. Nanda, N. Sood, B.V.K. Reddy, T.S. Markandeywar, Preparation and characterization of poly(vinyl alcohol)-chondroitin sulphate hydrogel as scaffolds for articular cartilage regeneration, Indian Journal of Materials Science 2013 (2013) 516021.

[41] A.K. Miri, H.G. Hosseinabadi, B. Cecen, S. Hassan, Y.S. Zhang, Permeability mapping of gelatin methacryloyl hydrogels, Acta Biomater. 77 (2018) 38–47.

[42] H.J. Yoon, S.R. Shin, J.M. Cha, S.-H. Lee, J.-H. Kim, J.T. Do, H. Song, H. Bae, Cold water fish gelatin methacryloyl hydrogel for tissue engineering application, PLoS One 11 (10) (2016) e0163902.

[43] S.R. Caliari, J.A. Burdick, A practical guide to hydrogels for cell culture, Nat. Methods 13 (5) (2016) 405–414.

[44] H.K. Heris, A.K. Miri, U. Tripathy, F. Barthelat, L. Mongeau, Indentation of poroviscoelastic vocal fold tissue using an atomic force microscope, J. Mech. Behav. Biomed. Mater. 28 (2013) 383–392.

[45] E.C. Beck, M. Barragan, M.H. Tadros, S.H. Gehrke, M.S. Detamore, Approaching the compressive modulus of articular cartilage with a decellularized cartilage-based hydrogel, Acta Biomater. 38 (2016) 94–105.

[46] H. Yin, M. Zhu, Y. Wang, L. Luo, Q. Ye, B.H. Lee, Physical properties and cellular responses of gelatin methacryloyl bulk hydrogels and highly ordered porous hydrogels, Frontiers in Soft Matter 2 (2023).

[47] Reproducing the Biomechanical Environment of the Chondrocyte for Cartilage Tissue Engineering, Tissue Eng. B Rev. 28 (2) (2022) 405–420.

[48] B. Bachmann, S. Spitz, B. Schädl, A.H. Teuschl, H. Redl, S. Nürnberger, P. Ertl, Stiffness matters: fine-tuned hydrogel elasticity alters chondrogenic redifferentiation, Front. Bioeng. Biotechnol. 8 (2020).
[49] C. Guimarães, L. Gasperini, A. Marques, R.L. Reis, The stiffness of living tissues and its implications for tissue engineering, Nat. Rev. Mater. 5 (2020).
[50] X. Li, S. Chen, J. Li, X. Wang, J. Zhang, N. Kawazoe, G. Chen, 3D culture of chondrocytes in gelatin hydrogels with different stiffness, Polymers 8 (8) (2016) 269.
[51] S. Pahoff, C. Meinert, O. Bas, L. Nguyen, T.J. Klein, D.W. Hutmacher, Effect of gelatin source and photoinitiator type on chondrocyte redifferentiation in gelatin methacryloyl-based tissue-engineered cartilage constructs, J. Mater. Chem. B 7 (10) (2019) 1761–1772.
[52] X. Zhao, Q. Lang, L. Yildirimer, Z.Y. Lin, W. Cui, N. Annabi, K.W. Ng, M. R. Dokmeci, A.M. Ghaemmaghami, A. Khademhosseini, Photocrosslinkable gelatin hydrogel for epidermal tissue engineering, Adv. Healthcare Mater. 5 (1) (2016) 108–118.
[53] B.D. Fairbanks, M.P. Schwartz, C.N. Bowman, K.S. Anseth, Photoinitiated polymerization of PEG-diacrylate with lithium phenyl-2,4,6-trimethylbenzoylphosphinate: polymerization rate and cytocompatibility, Biomaterials 30 (35) (2009) 6702–6707.
[54] S. Shahidi, M. Janmaleki, S. Riaz, A. Sanati Nezhad, N. Syed, A tuned gelatin methacryloyl (GelMA) hydrogel facilitates myelination of dorsal root ganglia neurons in vitro, Mater. Sci. Eng., C 126 (2021) 112131.
[55] E. Neto, C.J. Alves, L. Leitão, D.M. Sousa, I.S. Alencastre, F. Conceição, M. Lamghari, Axonal outgrowth, neuropeptides expression and receptors tyrosine kinase phosphorylation in 3D organotypic cultures of adult dorsal root ganglia, PLoS One 12 (7) (2017) e0181612.
[56] R. Mooney, A.A. Cole, K. Bjugstad, M.J. Mahoney, Development of porous PEG hydrogels that enable efficient, uniform cell-seeding and permit early neural process extension, Acta Biomater. 5 (2009) 1884–1897.
[57] V.A. Kornev, E.A. Grebenik, A.B. Solovieva, R.I. Dmitriev, P.S. Timashev, Hydrogel-assisted neuroregeneration approaches towards brain injury therapy: a state-of-the-art review, Comput. Struct. Biotechnol. J. 16 (2018) 488–502.
[58] L. Leitão, E. Neto, F. Conceição, A. Monteiro, M. Couto, C.J. Alves, D.M. Sousa, M. Lamghari, Osteoblasts are inherently programmed to repel sensory innervation, Bone Research 8 (1) (2020) 20.
[59] E. Neto, C.J. Alves, D.M. Sousa, I.S. Alencastre, A.H. Lourenço, L. Leitão, H. R. Ryu, N.L. Jeon, R. Fernandes, P. Aguiar, R.D. Almeida, M. Lamghari, Sensory neurons and osteoblasts: close partners in a microfluidic platform, Integr. Biol. 6 (6) (2014) 586–595.
[60] E. Neto, A.C. Monteiro, C. Leite Pereira, M. Simões, J.P. Conde, V. Chu, B. Sarmento, M. Lamghari, Micropathological chip modeling the neurovascular unit response to inflammatory bone condition, Adv. Healthcare Mater. 11 (11) (2022) e2102305.
[61] Dynamic mechanical loading enhances functional properties of tissue-engineered cartilage using mature canine chondrocytes, Tissue Eng. 16 (5) (2010) 1781–1790.
[62] Expansion and Redifferentiation of Chondrocytes from Osteoarthritic Cartilage: Cells for Human Cartilage Tissue Engineering, Tissue Eng. 15 (11) (2009) 3513–3523.
[63] A. Brandl, P. Angele, C. Roll, L. Prantl, R. Kujat, B. Kinner, Influence of the growth factors PDGF-BB, TGF-β1 and bFGF on the replicative aging of human articular chondrocytes during in vitro expansion, J. Orthop. Res. 28 (3) (2010) 354–360.
[64] M.M.J. Caron, P.J. Emans, M.M.E. Coolsen, L. Voss, D.A.M. Surtel, A. Cremers, L. W. van Rhijn, T.J.M. Welting, Redifferentiation of dedifferentiated human articular chondrocytes: comparison of 2D and 3D cultures, Osteoarthritis Cartilage 20 (10) (2012) 1170–1178.
[65] A. Barbero, S. Ploegert, M. Heberer, I. Martin, Plasticity of clonal populations of dedifferentiated adult human articular chondrocytes, Arthritis Rheum. 48 (5) (2003) 1315–1325.
[66] C.B. Carballo, Y. Nakagawa, I. Sekiya, S.A. Rodeo, Basic science of articular cartilage, Clin. Sports Med. 36 (3) (2017) 413–425.
[67] Z. Lin, J.B. Fitzgerald, J. Xu, C. Willers, D. Wood, A.J. Grodzinsky, M.H. Zheng, Gene expression profiles of human chondrocytes during passaged monolayer cultivation, J. Orthop. Res. 26 (9) (2008) 1230–1237.
[68] T. Lam, T. Dehne, J.P. Krüger, S. Hondke, M. Endres, A. Thomas, R. Lauster, M. Sittinger, L. Kloke, Photopolymerizable gelatin and hyaluronic acid for stereolithographic 3D bioprinting of tissue-engineered cartilage, J. Biomed. Mater. Res. B Appl. Biomater. 107 (8) (2019) 2649–2657.
[69] W. Bi, J.M. Deng, Z. Zhang, R.R. Behringer, B. de Crombrugghe, Sox9 is required for cartilage formation, Nat. Genet. 22 (1) (1999) 85–89.
[70] R.M. Borzí, E. Olivotto, S. Pagani, R. Vitellozzi, S. Neri, M. Battistelli, E. Falcieri, A. Facchini, F. Flamigni, M. Penzo, D. Platano, S. Santi, A. Facchini, K.B. Marcu, Matrix metalloproteinase 13 loss associated with impaired extracellular matrix remodeling disrupts chondrocyte differentiation by concerted effects on multiple regulatory factors, Arthritis Rheum. 62 (8) (2010) 2370–2381.
[71] K.G. Yang, D.B. Saris, R.E. Geuze, M.H. van Rijen, Y.J. van der Helm, A. J. Verbout, L.B. Creemers, W.J. Dhert, Altered in vitro chondrogenic properties of chondrocytes harvested from unaffected cartilage in osteoarthritic joints, Osteoarthritis Cartilage 14 (6) (2006) 561–570.
[72] Z. Lin, Z. Li, E.N. Li, X. Li, C.J. Del Duke, H. Shen, T. Hao, B. O'Donnell, B. A. Bunnell, S.B. Goodman, P.G. Alexander, R.S. Tuan, H. Lin, Osteochondral tissue chip derived from iPSCs: modeling OA pathologies and testing drugs, Front. Bioeng. Biotechnol. 7 (2019) 411.
[73] M.N. Ferrao Blanco, Y.M. Bastiaansen-Jenniskens, M.G. Chambers, A. A. Pitsillides, R. Narcisi, G. van Osch, Effect of inflammatory signaling on human articular chondrocyte hypertrophy: potential involvement of tissue repair macrophages, Cartilage 13 (2_suppl) (2021) 168s–174s.
[74] A.A.J. Hamers, H.Q. Dinh, G.D. Thomas, P. Marcovecchio, A. Blatchley, C. S. Nakao, C. Kim, C. McSkimming, A.M. Taylor, A.T. Nguyen, C.A. McNamara, C. C. Hedrick, Human monocyte heterogeneity as revealed by high-dimensional mass cytometry, Arterioscler. Thromb. Vasc. Biol. 39 (1) (2019) 25–36.
[75] M.B. Goldring, M. Otero, D.A. Plumb, C. Dragomir, M. Favero, K. El Hachem, K. Hashimoto, H.I. Roach, E. Olivotto, R.M. Borzì, K.B. Marcu, Roles of inflammatory and anabolic cytokines in cartilage metabolism: signals and multiple effectors converge upon MMP-13 regulation in osteoarthritis, Eur. Cell. Mater. 21 (2011) 202–220.
[76] Q. Hu, M. Ecker, Overview of MMP-13 as a promising target for the treatment of osteoarthritis, Int. J. Mol. Sci. 22 (4) (2021).
[77] P. Shen, S. Serve, P. Wu, X. Liu, Y. Dai, N. Durán-Hernández, D.T.M. Nguyen, M. Fuchs, T. Maleitzke, M.-J. Reisener, M. Dzamukova, K. Nussbaumer, T. M. Brunner, Y. Li, V. Holecska, G.A. Heinz, F. Heinrich, P. Durek, G. Katsoula, C. Gwinner, T. Jung, E. Zeggini, T. Winkler, M.-F. Mashreghi, M. Pumberger, C. Perka, M. Löhning, NOS inhibition reverses TLR2-induced chondrocyte dysfunction and attenuates age-related osteoarthritis, Proc. Natl. Acad. Sci. USA 120 (29) (2023) e2207993120.
[78] K. Yudoh, H. Nakamura, K. Masuko-Hongo, T. Kato, K. Nishioka, Erratum to: catabolic stress induces expression of hypoxia-inducible factor (HIF)-1α in articular chondrocytes: involvement of HIF-1α in the pathogenesis of osteoarthritis, Arthritis Res. Ther. 7 (5) (2005) 225.
[79] C.-Y. Zeng, X.-F. Wang, F.-Z. Hua, HIF-1α in osteoarthritis: from pathogenesis to therapeutic implications, Front. Pharmacol. 13 (2022).
[80] J. Miotla Zarebska, A. Chanalaris, C. Driscoll, A. Burleigh, R.E. Miller, A. M. Malfait, B. Stott, T.L. Vincent, CCL2 and CCR2 regulate pain-related behaviour and early gene expression in post-traumatic murine osteoarthritis but contribute little to chondropathy, Osteoarthritis Cartilage 25 (3) (2017) 406–412.
[81] S.B. Oh, P.B. Tran, S.E. Gillard, R.W. Hurley, D.L. Hammond, R.J. Miller, Chemokines and glycoprotein120 produce pain hypersensitivity by directly exciting primary nociceptive neurons, J. Neurosci. 21 (14) (2001) 5027–5035.
[82] A. Mukherjee, B. Das, The role of inflammatory mediators and matrix metalloproteinases (MMPs) in the progression of osteoarthritis, Biomaterials and Biosystems 13 (2024) 100090.
[83] S. Teufel, L. Wolff, U. König, A. Kobayashi, R. Behringer, C. Hartmann, Mice lacking Wnt9a or Wnt4 are prone to develop spontaneous osteoarthritis with age and display alteration in either the trabecular or cortical bone compartment, J. Bone Miner. Res. 37 (7) (2022) 1335–1351.
[84] J.C. Lui, S. Yue, A. Lee, B. Kikani, A. Temnycky, K.M. Barnes, J. Baron, Persistent Sox9 expression in hypertrophic chondrocytes suppresses transdifferentiation into osteoblasts, Bone 125 (2019) 169–177.
[85] A.R. Poole, M. Kobayashi, T. Yasuda, S. Laverty, F. Mwale, T. Kojima, T. Sakai, C. Wahl, S. El-Maadawy, G. Webb, E. Tchetina, W. Wu, Type II collagen degradation and its regulation in articular cartilage in osteoarthritis, Ann. Rheum. Dis. 61 (Suppl 2) (2002) ii78–81. Suppl 2.
[86] Z. Zou, X. Luo, Z. Chen, Y.S. Zhang, C. Wen, Emerging microfluidics-enabled platforms for osteoarthritis management: from benchtop to bedside, Theranostics 12 (2) (2022) 891–909.
[87] M. Morgan, J. Thai, V. Nazemian, R. Song, J.J. Ivanusic, Changes to the activity and sensitivity of nerves innervating subchondral bone contribute to pain in late-stage osteoarthritis, Pain 163 (2) (2022) 390–402.
[88] E. Neto, C.J. Alves, D.M. Sousa, I.S. Alencastre, A.H. Lourenço, L. Leitão, H. R. Ryu, N.L. Jeon, R. Fernandes, P. Aguiar, R.D. Almeida, M. Lamghari, Sensory neurons and osteoblasts: close partners in a microfluidic platform, Integr. Biol. 6 (6) (2014) 586–595.
[89] B.A. Lázár, G. Jancsó, P. Sántha, Modulation of sensory nerve function by insulin: possible relevance to pain, inflammation and axon growth, Int. J. Mol. Sci. 21 (7) (2020).
[90] H. Yako, N. Niimi, A. Kato, S. Takaku, Y. Tatsumi, Y. Nishito, K. Kato, K. Sango, Role of pyruvate in maintaining cell viability and energy production under high-glucose conditions, Sci. Rep. 11 (1) (2021) 18910.
[91] C. Gomez, B. Burt-Pichat, F. Mallein-Gerin, B. Merle, P.D. Delmas, T.M. Skerry, L. Vico, L. Malaval, C. Chenu, Expression of Semaphorin-3A and its receptors in endochondral ossification: potential role in skeletal development and innervation, Dev. Dynam. 234 (2) (2005) 393–403.
[92] M. Okubo, T. Kimura, Y. Fujita, S. Mochizuki, Y. Niki, H. Enomoto, Y. Suda, Y. Toyama, Y. Okada, Semaphorin 3A is expressed in human osteoarthritic cartilage and antagonizes vascular endothelial growth factor 165–promoted chondrocyte migration: an implication for chondrocyte cloning, Arthritis Rheum. 63 (10) (2011) 3000–3009.
[93] H.J. Im, X. Li, P. Muddasani, G.H. Kim, F. Davis, J. Rangan, C.B. Forsyth, M. Ellman, E.J. Thonar, Basic fibroblast growth factor accelerates matrix degradation via a neuro-endocrine pathway in human adult articular chondrocytes, J. Cell. Physiol. 215 (2) (2008) 452–463.
[94] M.A.M. Vis, K. Ito, S. Hofmann, Impact of culture medium on cellular interactions in in vitro Co-culture systems, Front. Bioeng. Biotechnol. 8 (2020).
[95] M. Rothbauer, H. Zirath, P. Ertl, Recent advances in microfluidic technologies for cell-to-cell interaction studies, Lab Chip 18 (2) (2018) 249–270.
[96] C. Sumi, N. Hirose, M. Yanoshita, M. Takano, S. Nishiyama, Y. Okamoto, Y. Asakawa, K. Tanimoto, Semaphorin 3A inhibits inflammation in chondrocytes under excessive mechanical stress, Mediat. Inflamm. 2018 (2018) 5703651.
[97] N.P. Boyer, S.L. Gupton, Revisiting netrin-1: one who guides (axons), Front. Cell. Neurosci. 12 (2018).

[98] S. Zhu, J. Zhu, G. Zhen, Y. Hu, S. An, Y. Li, Q. Zheng, Z. Chen, Y. Yang, M. Wan, R. L. Skolasky, Y. Cao, T. Wu, B. Gao, M. Yang, M. Gao, J. Kuliwaba, S. Ni, L. Wang, C. Wu, D. Findlay, H.K. Eltzschig, H.W. Ouyang, J. Crane, F.Q. Zhou, Y. Guan, X. Dong, X. Cao, Subchondral bone osteoclasts induce sensory innervation and osteoarthritis pain, J. Clin. Invest. 129 (3) (2019) 1076–1093.
[99] M. Cai, Q. Zheng, Y. Chen, S. Liu, H. Zhu, B. Bai, Insights from the neural guidance factor Netrin-1 into neurodegeneration and other diseases, Front. Mol. Neurosci. 17 (2024) 1379726.
[100] R. Wehrle, E. Camand, A. Chedotal, C. Sotelo, I. Dusart, Expression of netrin-1, slit-1 and slit-3 but not of slit-2 after cerebellar and spinal cord lesions, Eur. J. Neurosci. 22 (9) (2005) 2134–2144.
[101] M.A. Riyadh, Y. Shinmyo, K. Ohta, H. Tanaka, Inhibitory effects of draxin on axonal outgrowth and migration of precerebellar neurons, Biochem. Biophys. Res. Commun. 449 (1) (2014) 169–174.
[102] Y. Shinmyo, M. Asrafuzzaman Riyadh, G. Ahmed, I. Bin Naser, M. Hossain, H. Takebayashi, H. Kawasaki, K. Ohta, H. Tanaka, Draxin from neocortical neurons controls the guidance of thalamocortical projections into the neocortex, Nat. Commun. 6 (1) (2015) 10232.
[103] D.K. Unni, M. Piper, R.X. Moldrich, I. Gobius, S. Liu, T. Fothergill, A.-L. S. Donahoo, J.M. Baisden, H.M. Cooper, L.J. Richards, Multiple Slits regulate the development of midline glial populations and the corpus callosum, Dev. Biol. 365 (1) (2012) 36–49.
[104] H. Kim, Y.-J. Choi, Y.-S. Lee, S.Y. Park, J.-E. Baek, H.-K. Kim, B.-J. Kim, S.H. Lee, J.-M. Koh, SLIT3 regulates endochondral ossification by β-catenin suppression in chondrocytes, Biochem. Biophys. Res. Commun. 506 (4) (2018) 847–853.
[105] T. Schubert, S. Kaufmann, A.K. Wenke, S. Grässel, A.K. Bosserhoff, Role of deleted in colon carcinoma in osteoarthritis and in chondrocyte migration, Rheumatology 48 (11) (2009) 1435–1441.
[106] Z. Matharu, D. Patel, Y. Gao, A. Haque, Q. Zhou, A. Revzin, Detecting transforming growth factor-β release from liver cells using an aptasensor integrated with microfluidics, Anal. Chem. 86 (17) (2014) 8865–8872.
[107] Z.T.F. Yu, H. Guan, M.K. Cheung, W.M. McHugh, T.T. Cornell, T.P. Shanley, K. Kurabayashi, J. Fu, Rapid, automated, parallel quantitative immunoassays using highly integrated microfluidics and AlphaLISA, Sci. Rep. (2015) 11339.
[108] N. Momenbeitollahi, T. Cloet, H. Li, Pushing the detection limits: strategies towards highly sensitive optical-based protein detection, Anal. Bioanal. Chem. 413 (24) (2021) 5995–6011.
[109] Y. Liao, Y. Ren, X. Luo, A.J. Mirando, J.T. Long, A. Leinroth, R.-R. Ji, M.J. Hilton, Interleukin-6 signaling mediates cartilage degradation and pain in posttraumatic osteoarthritis in a sex-specific manner, Sci. Signal. 15 (744) (2022) eabn7082.
[110] M.J. Pearson, D. Herndler-Brandstetter, M.A. Tariq, T.A. Nicholson, A.M. Philp, H.L. Smith, E.T. Davis, S.W. Jones, J.M. Lord, IL-6 secretion in osteoarthritis patients is mediated by chondrocyte-synovial fibroblast cross-talk and is enhanced by obesity, Sci. Rep. 7 (1) (2017) 3451.
[111] S. Liu, Z. Deng, K. Chen, S. Jian, F. Zhou, Y. Yang, Z. Fu, H. Xie, J. Xiong, W. Zhu, Cartilage tissue engineering: from proinflammatory and anti-inflammatory cytokines to osteoarthritis treatments, Mol. Med. Rep. 25 (3) (2022) 99 (Review).
[112] T. Mabey, S. Honsawek, A. Tanavalee, P. Yuktanandana, V. Wilairatana, Y. Poovorawan, Plasma and synovial fluid inflammatory cytokine profiles in primary knee osteoarthritis, Biomarkers 21 (7) (2016) 639–644.
[113] R.E. Miller, P.B. Tran, S. Ishihara, D. Syx, D. Ren, R.J. Miller, A.M. Valdes, A. M. Malfait, Microarray analyses of the dorsal root ganglia support a role for innate neuro-immune pathways in persistent pain in experimental osteoarthritis, Osteoarthritis Cartilage 28 (5) (2020) 581–592.
[114] D.A. Walsh, D.F. McWilliams, M.J. Turley, M.R. Dixon, R.E. Fransès, P.I. Mapp, D. Wilson, Angiogenesis and nerve growth factor at the osteochondral junction in rheumatoid arthritis and osteoarthritis, Rheumatology 49 (10) (2010) 1852–1861.
[115] F. Iannone, C. De Bari, F. Dell'Accio, M. Covelli, V. Patella, G. Lo Bianco, G. Lapadula, Increased expression of nerve growth factor (NGF) and high affinity NGF receptor (p140 TrkA) in human osteoarthritic chondrocytes, Rheumatology 41 (12) (2002) 1413–1418.
[116] L. Aloe, M.L. Rocco, P. Bianchi, L. Manni, Nerve growth factor: from the early discoveries to the potential clinical use, J. Transl. Med. 10 (1) (2012) 239.
[117] H.M. Han, T.H. Kim, J.Y. Bae, Y.C. Bae, Primary sensory neurons expressing tropomyosin receptor kinase A in the rat trigeminal ganglion, Neurosci. Lett. 690 (2019) 56–60.
[118] R.-Y. Liu, R.-S. Schmid, W.D. Snider, P.F. Maness, NGF enhances sensory axon growth induced by laminin but not by the L1 cell adhesion molecule, Mol. Cell. Neurosci. 20 (1) (2002) 2–12.
[119] K.M. Mearow, Y. Kril, Anti-NGF treatment blocks the upregulation of NGF receptor mRNA expression associated with collateral sprouting of rat dorsal root ganglion neurons, Neurosci. Lett. 184 (1) (1995) 55–58.
[120] Y. Jiang, R.S. Tuan, Role of NGF-TrkA signaling in calcification of articular chondrocytes, Faseb. J. 33 (9) (2019) 10231–10239.
[121] L. Farinelli, M. Barba, B. Beltrami, M. Baranzini, D. Milani, W. Lattanzi, S. Manzotti, A. Gigante, Effects of NGF and BDNF on chondrocytes: a microarray analysis, J. Biol. Regul. Homeost. Agents 34 (4 Suppl. 3) (2020) 83–89. Congress of the Italian Orthopaedic Research Society.